Tailoring Porosity in Copper-Based Multinary Sulfide Nanostructures for Energy, Biomedical, Catalytic and Sensing Applications

Michelle D. Regulacio, Yong Wang, Zhi Wei Seh and Ming-Yong Han*

Institute of Materials Research and Engineering (IMRE), Agency for Science, Technology and Research (A*STAR), 2 Fusionopolis Way, Innovis, Singapore 138634

KEYWORDS: multinary chalcogenide, copper sulfide, nanoparticle, porous, solution-phase

ABSTRACT: Copper-based multinary sulfides (CMS) have been the subject of intense research over the past decade due to the numerous outstanding properties that emerge when they are synthesized on the nanoscale. While many of these compounds (e.g. $CuInS_2$, Cu_2SnS_3, $Cu_{12}Sb_4S_{13}$ and Cu_2ZnSnS_4) are best known for their immense potential in energy-related disciplines, nanoscale engineering has opened up new and exciting opportunities for these materials to be used in a wider range of applications. This review accords particular attention to nanostructured CMS materials with porous morphological features to be used in energy, biomedical, catalytic and sensing applications, owing to their large, tunable and accessible surface area. While the construction of porous nanostructures of metals and binary materials has already been well established, tailoring porosity in multinary materials like CMS remains a big challenge due to their multiple elemental components. Herein, we provide useful discussions on the different modes of pore formation that are fundamental to the construction of CMS nanostructures with tailor-made porosity. These pore-

forming strategies are classified into three types: (1) Kirkendall-effect-induced hollowing, (2) aggregation-based pore formation, and (3) template-assisted pore engineering. The ability to craft porous features in CMS nanomaterials has proven to be beneficial in advancing their properties and expanding their application domains, and so future efforts should be devoted to furthering our understanding of the various pore formation mechanisms as this could lead to the construction of more sophisticated porous CMS architectures with optimal performance for desired applications. We anticipate that the design concepts discussed here can be extended to other emerging classes of multinary materials.

1. Introduction

1.1. Copper-based multinary sulfides (CMS)

Binary copper sulfides are an important class of inorganic materials that have attracted tremendous amount of attention from various scientific communities globally. With their remarkable intrinsic properties, low toxicity and widespread availability, they have found practical utility in many areas of modern science and technology.[1–4] These compounds, which are generally represented by the formula $Cu_{2-x}S$ (where x = 1–2), exist in a variety of stoichiometries that range from Cu_2S to CuS, with several off-stoichiometric compositions in between (e.g. $Cu_{1.96}S$, $Cu_{1.8}S$, $Cu_{1.75}S$, $Cu_{1.12}S$).[4] The crystallographic structure and the band gap vary depending on the $Cu_{2-x}S$ stoichiometry and so composition control can be used to modulate their properties. Interestingly, addition of one or more elemental constituents to the basic binary Cu–S system to form complex multinary compositions can provide even greater flexibility in the tuning of properties and could well be a key to achieving optimal performance for desired functions. This has stimulated growing interest in the multinary derivatives of copper sulfide, which will be referred to in this review as copper-based multinary sulfides (CMS).

Elements of the p-block (e.g. In, Ga, Al, Sn, Ge, Sb, Bi), d-block (e.g. Zn, Fe, Co, Ni, Mo), and f-block (e.g. La, Nd, Sm, Eu, Tb) can all be utilized to form multinary compounds with copper sulfide. Considering the numerous possible compositions and crystal structures attainable when these elements are incorporated into the Cu–S system, a vast library of CMS-based materials has emerged and it is continuously growing. Two of the most extensively studied are ternary $CuInS_2$ and quaternary Cu_2ZnSnS_4. These technologically promising semiconductors exemplify the compositional and structural versatility that are inherent characteristics of the CMS compounds. For instance, $CuInS_2$ is capable of tolerating a wide range of off-stoichiometric compositions that can be finely tuned to improve its emission properties. A considerable enhancement in photoluminescence efficiency has been achieved for the Cu-deficient and In-rich compositions.[5–7] This makes them appealing as optically active materials for lighting and imaging applications. CMS materials can also accommodate dopants or form alloys with other semiconductors that can alter their band structure. For example, when $CuInS_2$ is alloyed with the wide-gap semiconductor ZnS in varying ratios, a series of quaternary $(CuInS_2)_{1-x}(ZnS)_x$ alloys having composition-dependent band gaps are produced.[8] The ZnS-rich compositions have been shown to absorb visible photons more effectively than the unalloyed $CuInS_2$ and they have been successfully utilized in visible-light-induced photocatalysis.[9,10] Meanwhile, improved solar cell conversion efficiencies have been reported when Cu_2ZnSnS_4 is alloyed with its Ge (Cu_2ZnGeS_4) and Se ($Cu_2ZnSnSe_4$) counterparts to form the quinary compounds $Cu_2ZnSn_{1-x}Ge_xS_4$ and $Cu_2ZnSn(S_{1-x}Se_x)_4$, respectively.[11–13] CMS compounds are also known to possess crystallographically diverse structures. In the case of $CuInS_2$, it has three known polymorphic forms: the chalcopyrite, zinc-blende, and wurtzite structures.[14] Recent studies have revealed that a new type of cation ordering, called interlacing, exists in the wurtzite

polymorph of $CuInS_2$.[15] This kind of ordering reduces phonon conductivity, making wurtzite-phase $CuInS_2$ highly attractive for thermoelectrics.

Undeniably, the compositional and structural diversity of CMS compounds are beneficial to the advancement of their properties. However, the main challenge lies in the development of convenient and reliable synthetic methodologies that could allow for precise tuning of their composition and crystal structure. Many scientists have relied heavily on solution-phase synthetic approaches (e.g. hydrothermal/solvothermal technique, colloidal chemical method) because of their potential to control not only the composition and crystal phase, but also the size and morphology of materials.[1,16–23] The materials that are synthesized in solution are typically nanoscale structures (i.e., nanostructures) with size- and morphology-dependent properties that are not observed in the bulk solids. Therefore, nanoscale engineering through controlled synthesis in solution provides additional options for property tuning that can be exploited in the rational design of functional CMS-based materials toward desired applications.

1.2. Porosity in nanostructures

Over the past decades, an extensive array of nanostructure morphologies has been developed for different inorganic materials with the goal of modifying properties to suit specific applications. The morphologies range from simple shapes like rods and plates, to more complex architectures, such as flowers and cages. Porosity is a morphological feature that is often sought-after due to the many advantages that it can bring when incorporated into the nanoscale architecture. As the name implies, porous nanostructures are characterized by the presence of pore/s. The pore could be a single large void at the core like in the case of hollow structures (e.g. hollow spheres, tubes, boxes),[24–30] or could be numerous, small and randomly distributed, such as in three-dimensional (3D) hierarchically-assembled architectures (e.g. flower-like and sponge-

like structures).[31–35] Complex porous nanostructures such as those that have hollow interiors and mesoporous shells (i.e., with one huge void at the center and several smaller voids at the exterior) have also been fabricated for a wide variety of materials in recent years.[36–40]

With the existence of void spaces, porous nanostructures have higher surface-to-volume ratio and lower density as compared to their pore-free counterparts of the same size, and these properties render them attractive for use in many important applications, which include catalysis, sensing, drug delivery and energy storage.[36–59] In the field of catalysis, porosity is favorable because the larger surface area possessed by porous nanostructures translates to more available active sites for catalytic reactions, while their good surface permeability promotes diffusion and transport of molecules that leads to better contact of guest molecules with more active surfaces.[41–46] For similar reasons, porosity is advantageous in sensing applications where low diffusion barriers, improved mass transport and large numbers of adsorption sites for target molecules are desired.[47–50] The cavities in porous nanostructures can also enable loading, storage and transport of different cargoes. For instance, pore-containing nanostructures can serve as drug delivery carriers with their ability to encapsulate drug molecules and regulate the release of these drugs to selectively target diseased tissues.[51–54] Porous nanomaterials are also ideal electrode materials for energy storage systems like rechargeable batteries and supercapacitors because their void spaces can alleviate the structural strain during charge-discharge cycling.[55–57] Porosity also allows for efficient electrolyte penetration, facilitates rapid transport of ions and electrons, and provides richer electroactive sites for redox reactions, leading to superior electrochemical performance.[58,59] Suffice it to say that there is much potential benefit that can be derived from a porous morphology, and so a great deal of research is currently directed toward the study and understanding of porous nanomaterials.

1.3. Scope of review

The substantial growth seen each year in the number of publications on CMS compounds is proof that research on this evolving class of inorganic materials is rapidly progressing. The high level of interest in these compounds is largely attributed to the remarkable properties observed in their nanostructured forms. In this review, we aim to show how a porous nanostructure morphology can help enhance their properties and offer exciting opportunities for them to be utilized in an extensive range of applications. Section 2 is entirely devoted to the strategies that have been successfully employed in fabricating porous CMS nanostructures to orient the readers on how these materials are constructed. Because of the high degree of complexity in synthesizing multinary materials, creating CMS nanostructures with tailor-made porosity can be extremely daunting, but one can overcome this difficulty when equipped with sufficient knowledge of the different pore formation processes. Pictorial representations are aptly provided to aid the readers in visualizing the processes and the structures described. In Section 3, we illustrate how a porous architecture can be used to modify properties and deliver specific functions toward desired applications. The applicability of porous CMS nanostructures in biomedicine, energy storage, catalysis, and sensing are highlighted. Lastly, a summary is provided together with the main conclusions and outlook in the final section.

2. Strategies for creating porous CMS nanostructures

It is generally acknowledged that the judicious selection of synthetic conditions is fundamental to attaining precise control of nanostructure morphology. In creating porous nanostructures, different solution-phase synthetic protocols have been employed, and the final porous morphology is determined by the mechanism of pore formation that operates under particular reaction conditions. In this section, we present the different pore formation mechanisms that have effectively produced

porous CMS nanostructures in solution. For ease of discussion, we have classified them into three types: (1) Kirkendall-effect-induced hollowing, (2) aggregation-based pore formation, and (3) template-assisted pore engineering. Table 1 provides a summary of the various porous CMS nanostructures that have been fabricated through these strategies.

2.1. Kirkendall-effect-induced hollowing

The Kirkendall effect arises when diffusion is allowed to take place between two adjacent solids that have different diffusivities.[26] Because of the unequal diffusion rates, there is a net movement of atoms from one side of the interface to the other. With the atoms diffusing to one direction, a balance is achieved by an equal net flow of vacancies to the opposite direction. When the concentration of atomic vacancies reach supersaturation, the vacancies merge to form voids and this induces porosity in the solid. This phenomenon was first discovered in the 1940's in Ernest Kirkendall's laboratory, where it was observed that at elevated temperatures, the inequality of the diffusion rates of copper and zinc led to an interface shift and pore formation in a copper-plated bar of brass.[60]

Through a vacancy diffusion mechanism analogous to the Kirkendall effect, interior pores can form within a nanocrystal when the elemental components have different diffusion rates. Termed as nanoscale Kirkendall effect, this process of pore formation in nanometer-sized materials has been first exploited by Alivisatos et al. in their fabrication of colloidal hollow nanocrystals, where a clearly defined void is produced in the central interior region of each nanocrystal.[61] In their highly-cited work, hollow cobalt chalcogenide nanocrystals are created when a solution of the chalcogen precursor in organic solvent is injected into a dispersion of pre-synthesized cobalt nanocrystals at 182 °C. The use of the hot-injection synthetic approach is instrumental in facilitating the formation of an intermediate core–shell structure within which the Kirkendall-type diffusion takes place. For

example, in the case of cobalt sulfide, the injected sulfur first reacts with the surface atoms of the pre-existing cobalt nanocrystals to create a cobalt sulfide coating. This consequently gives rise to a heterogeneous solid structure comprising of a cobalt core and a cobalt sulfide shell. Further reaction of the cobalt core with the sulfur precursor is hindered by the outer cobalt sulfide shell, and so its complete conversion to cobalt sulfide proceeds through the interdiffusion of cobalt and sulfur atoms across the core–shell interface. Because the outward diffusion of cobalt atoms is faster than the inward diffusion of sulfur atoms, vacancies are generated at the core and this eventually leads to cobalt sulfide nanocrystals having hollow interiors.

Following the work done by the Alivisatos group on nanoscale Kirkedall effect, significant progress has been achieved in the synthesis of hollow nanostructures of several binary compounds, particularly of metal oxides, chalcogenides, and phosphides.[26,62,63] In the case of multinary compounds, the formation of hollow nanostructures is more challenging because the unequal atomic diffusion becomes more complicated in compounds with more than two elemental components. Nevertheless, there have been recent reports on the successful application of the Kirkendall-type pore formation on multinary chalcogenide nanocrystals. For instance, the Kirkendall-effect-induced hollowing has been effectively demonstrated by Dong et al. in their colloidal synthesis of hollow Cu_2GeS_3 nanocrystals from Cu–TGA and Ge–TGA precursors (where TGA is the thioglycolic acid ligand, $HSCH_2COO^-$).[64] The key is to use metal precursors with different reactivities so that the nucleation of the different metal components does not happen simultaneously. As schematically depicted in Figure 1a, the process leading to the formation of hollow Cu_2GeS_3 nanostructures begins with the nucleation of Cu_7S_4 upon decomposition of the more reactive Cu–TGA precursor as the reaction mixture was heated to 300 °C. This is followed by the decomposition of the Ge–TGA complex, which generates a thin layer of GeS_2 coating on the pre-formed Cu_7S_4 seeds. Interdiffusion

of Cu^{+} and Ge^{4+} subsequently takes place, with the more mobile Cu^{+} ions diffusing more rapidly than Ge^{4+}. The interdiffusion of metal ions gives rise to a layer of ternary Cu_2GeS_3 that forms in between the inner Cu_7S_4 core and the outer GeS_2 shell. As the reaction progresses, the GeS_2 shell vanishes as it is converted into the growing Cu_2GeS_3 layer, and vacancies are gradually created at the center due to the faster outward diffusion of Cu^{+} relative to the inward diffusion of Ge^{4+}. When the Cu^{+} ions from the Cu_7S_4 core have diffused completely, its sulfur sublattice disappears through diffusion or dissolution as it is unable to exist alone, thereby leaving a hollow interior. Transmission electron microscopy (TEM) measurements (Figure 1b,c) showed that the as-prepared hollow Cu_2GeS_3 nanostructures are nearly spherical in shape, with an average outer diameter of 16.7 nm and an average inner diameter of 6.9 nm. From X-ray diffraction (XRD) analysis, the resulting Cu_2GeS_3 was found to exhibit the wurtzite crystal structure, which is based on a hexagonal close-packed array of sulfur anions. It can be noted that a similar sulfur anion arrangement exists in monoclinic Cu_7S_4, which is the binary copper sulfide phase that forms at the initial stage of the reaction. In a more recent paper by Dong et al., it was revealed that the sulfur anion framework of the starting $Cu_{2-x}S$ nuclei actually plays a critical role in determining the crystal phase of the final Cu_2GeS_3 nanostructures.[65] By employing a synthetic protocol that produces cubic-phase $Cu_{7.2}S_4$ nuclei instead of monoclinic Cu_7S_4, they were able to prepare hollow Cu_2GeS_3 nanostructures with the cubic crystal structure. In this case, the sulfur anions in both the starting $Cu_{7.2}S_4$ seed and the resulting Cu_2GeS_3 are in a cubic-close packed arrangement. Generally speaking, the Kirkendall-type formation of hollow Cu_2GeS_3 nanostructures is a result of the unequal rates of diffusion of Cu^{+} and Ge^{4+} within the same sulfur anion framework of the nanocrystal lattice.

In their hot-injection synthesis of $CuInS_2$ nanoplates, Mu and co-workers have shown that the Kirkendall-effect-induced hollowing process can be controlled in a reaction-limited regime through

several factors such as the reactivity of indium precursor, the reaction temperature, and the size of the initial $Cu_{2-x}S$ seeds.[66] Starting with hexagonal-phase Cu_2S nanoplates, they have produced wurtzite-phase $CuInS_2$ nanoplates with either hollowed or solid morphology depending on whether the Kirkendall-type void formation has been activated or not after the injection of the indium precursor. In order to activate the nanoscale Kirkendall effect, the incorporation rate of In^{3+} into the Cu_2S nanoplates should be slow enough as to limit the availability of In^{3+} for inward diffusion. This would then allow the outward diffusion of Cu^+ to outcompete the inward diffusion of In^{3+}. For hollowing to occur, it is therefore necessary to have high reaction barriers for the insertion of In^{3+} into the nanocrystal lattice, and this is achieved with the use of less reactive indium precursors and low reaction temperatures. For example, hollow $CuInS_2$ nanoplates are formed when the starting Cu_2S nanoplates were reacted with InI_3 at 150 °C, whereas solid $CuInS_2$ nanoplates are obtained when the reaction was done at 200 °C with $InCl_3$. The nanoscale Kirkendall effect can also be regulated by the size of the starting Cu_2S material. Cu_2S seeds of larger dimensions are more susceptible to Kirkendall-type hollowing because the longer diffusion distance in larger Cu_2S nanocrystals lowers the effective inward diffusion rate of In^{3+}.

2.2. Aggregation-based pore formation

Colloidal nanocrystals are known to spontaneously aggregate under particular reaction conditions and this has enabled the construction of larger secondary structures (i.e., superstructures) with intricate morphologies.[67–71] A porous architecture is one of the remarkably complex morphologies that can result from nanocrystal aggregation. Different from the Kirkendall-type pore formation where singly-voided nanocrystals are typically produced, the aggregation-based process often results in a mesoporous structure where multiple pores are present. While there is complexity in the structure created, the mechanism behind aggregation-based pore formation is quite simple. In

general, empty spaces are generated as the accumulating nanocrystals coalesce and these interstices bring porosity to the secondary structure.

Oftentimes, the aggregation-induced pore formation leads to huge 3D hierarchically-assembled porous structures with noticeable nanocrystal components. For example, through a surfactant-less solvothermal synthetic strategy, Liang et al. have demonstrated that the self-aggregation of pre-formed Cu_2SnS_3 seeds can eventually lead to mesoporous flower-like Cu_2SnS_3 hierarchical architectures as shown in Figure 2a.[72] The Cu_2SnS_3 seeds are first nucleated from the reaction of metal chloride precursors with thiourea in ethylene glycol under solvothermal conditions at 180 °C. Because no surfactants are used in the synthesis, the primary Cu_2SnS_3 nuclei in the solution are unstable and are thus inclined to agglomerate and grow into larger structures. The growth process actually involves two stages of aggregation. The first stage produces two-dimensional (2D) Cu_2SnS_3 nanoflakes (or nanosheets) upon self-assembly of several primary Cu_2SnS_3 nanocrystals. These 10-nm thick nanoflakes are mesoporous and polycrystalline in nature as revealed by high-resolution TEM (HRTEM) analysis. The HRTEM image in Figure 2b shows grain boundaries as well as empty spaces or pores (lighter contrast regions highlighted by red arrows) between crystallite components that are 3 to 5 nm in size. The Cu_2SnS_3 nanoflakes then undergo a second aggregation process that generates the micrometer-sized flowers seen in Figure 2c. In the final product, the nanoflakes are the petals that constitute the multi-layered flower-like structures. Through a similar aggregative growth mechanism, 3D sponge-like $CuInS_2$ superstructures have been solvothermally produced by Liu et al.[73] The spherical sponge-like architectures resulted from the self-assembly of small nanosheets, which in turn are formed from the self-aggregation of small nanocrystals that are 7 to 8 nm in diameter.

In addition to the ternary CMS materials discussed above, the aggregation-driven formation of

3D hierarchical mesoporous structures has also been demonstrated for several quaternary CMS compounds, such as Cu_2MSnS_4 (M = Mn, Fe, Co, Ni, Zn and Cd)[74–80] and alloyed $(CuInS_2)_{1-x}(ZnS)_x$.[81,82] There are cases where the 2D nanoflakes (or nanosheets) that make up the final 3D architectures are found to exhibit high crystallinity where the nanocrystal subunits are mostly oriented. These were predominantly observed in the samples synthesized at higher temperatures for prolonged periods of time.[79,80] Zhou et al. have noted that because of the long heating durations, the crystalline state of the nanoflakes can gradually change from polycrystalline to single-crystalline via the grain rotation-induced grain coalescence mechanism.[80] However, even if the nanoflakes are single-crystalline, the final 3D superstructures are not because the nanoflakes comprising them are randomly arranged.

In some cases, aggregative growth leads to 3D mesoporous structures that are entirely single-crystalline despite the existence of voids.[83–85] This occurs as a result of oriented attachment, which is a non-classical crystal growth process where the randomly aggregated primary crystallites in a cluster self-organize to achieve crystallographic alignment before firmly attaching to one another.[86–88] Following attachment, atoms diffuse and rearrange to eliminate defects and interparticle boundaries, ultimately yielding secondary structures that are of single-crystal quality. In a recent work by Regulacio et al., unique multiply-voided $Cu_{12}Sb_4S_{13}$ nanotetrahedrons are generated via the oriented attachment mechanism.[89] As schematically illustrated in Figure 3a, the porous $Cu_{12}Sb_4S_{13}$ nanotetrahedrons are evolved from smaller oval-shaped $Cu_{12}Sb_4S_{13}$ nanocrystals. These primary nanocrystals are formed earlier in the reaction when $Cu(dedtc)_2$ and $Sb(dedtc)_3$ (where dedtc is the diethyldithiocarbamate ligand, $S_2CNEt_2^-$) are solvothermally heated in a solvent mixture of oleylamine and dodecanethiol. With continued heating, the primary nanocrystals aggregate to form loosely bound clusters that take the shape of a tetrahedron. The nanocrystals

subsequently rotate and rearrange themselves until crystallographic alignment is reached. Once aligned, attachment occurs and this ultimately leads to single-crystalline nanotetrahedrons having multiple pores (Figure 3b-c). It is worth noting that the mineral name of $Cu_{12}Sb_4S_{13}$ is tetrahedrite because tetrahedron is the known crystal habit of this material. It is thus not surprising that the pre-formed oval-shaped $Cu_{12}Sb_4S_{13}$ nanocrystals are inclined to merge and grow into tetrahedron-shaped nanostructures.

The TEM images in Figure 3a show that the surface texture and porosity of the nanotetrahedrons can be tuned by changing the reaction temperature. When the solvothermal synthesis was conducted at 80 °C for 16 h, the nanotetrahedrons that were obtained are predominantly grape-like in appearance with rough surface texture and seemingly interconnected pores. By contrast, the nanotetrahedrons obtained at 200 °C are substantially more compact, with fairly smooth surface texture and distinctive sphere-like voids (highlighted in Figure 3b). The existence of voids in the final nanostructures is a consequence of incomplete merging due to steric hindrance effects from the organic coordinating solvents that are bound to the nanocrystal surface. Both oleylamine and dodecanethiol have long alipathic chains that can restrict close contact between coalescing primary nanocrystals and increase the energy barrier for atomic diffusion. Because particle coalescence and atom diffusion can be promoted at elevated temperatures, increasing the solvothermal temperature leads to denser nanotetrahedrons with reduced porosity and smoother surface texture.

2.3. Template-assisted pore engineering

Another means of facilitating the formation of porous nanostructures is to use suitable templates that can serve as structural scaffolds for the incorporation of the desired porosity.[35–37,41–43,90] In many cases, the porous nanostructures that are produced have huge hollow interiors and multiply-voided rough-textured exteriors because the manner of growth is often through particle

aggregation on the template surface or on the template pore walls. The template materials can be generally classified into two types: hard templates and soft templates. Examples of how porous CMS nanostructures have been fabricated using these two types of template materials are provided in the subsections below.

2.3.1. Hard templates

Hard templates are rigid materials that possess specific shapes from which the morphology of the porous nanostructures is fashioned.[41–43] The creation of porous nanostructures through the hard-templating technique is very straightforward. The template material is prepared first, and then the desired material is allowed to form and grow either within or around the template into a shape that is complementary to that of the template. The last step usually involves the complete removal of the template or, in the case of sacrificial hard templates,[91–94] the transformation of the template into the final porous product.

Using porous anodic aluminum oxide (AAO) as template, Su and co-workers have fabricated Cu_2ZnSnS_4 nanotubes through a sol-gel synthetic process.[95] The synthetic steps are shown schematically in Figure 4a. First, the pre-made AAO template was immersed in the sol-gel precursor solution, which consists of the metal salts, thiourea, and 2-methoxyethanol. This resulted in the filling of the 200-nm-sized pores of AAO by the sol-gel mixture. With a glass slide placed underneath, the filled template was then taken out of the precursor solution, and the sol-gel system contained within the pores was allowed to adsorb onto the pore walls using filter paper linings. Annealing at 550 °C in sulfur atmosphere yielded Cu_2ZnSnS_4 nanotubes, which were subsequently released from the template through selective etching of AAO using aqueous NaOH solution. Nanotubes are one-dimensional (1D) cylindrical nanostructures having hollow interiors. When the sol-gel mixture was not made to adsorb onto the pore walls prior to annealing, solid Cu_2ZnSnS_4

nanowires were obtained instead. Thus, the adsorption step is pivotal to the creation of a hollow interior that distinguishes a nanotube from a nanowire. The TEM image of a representative nanotube is shown in the inset of Figure 4a. The tube diameter is about 200 nm, which is in agreement with the pore diameter of the AAO template. Meanwhile, the length of the nanotubes is measured to be 60 μm and this matches the thickness of the template. The use of AAO as a hard template was also adopted by Shi et al. in their template-directed synthesis of tubular $CuInS_2$ nanomaterials.[96] $CuInS_2$ nanotubes that are open-ended on both sides were produced when both ends of the AAO pores are left open, while a test tube-like morphology was generated by closing one end of the AAO pores. A uniform size distribution was observed where the average outer diameter of the tubes equals the template pore size dimension.

Self-sacrificial hard-templating is another way of preparing porous CMS nanostructures. This has been successfully demonstrated by Lin and co-workers in their fabrication of ternary Cu–Sn–S composite nanotubes through a gelation–solvothermal technique, where *in situ* generated CuCl–thiourea nanotubes served as the sacrificial hard template.[97] The formation process, as schematically presented in Figure 4b, proceeds via an *in situ* transformation mechanism by which the 1D tubular structure of the sacrificial template is inherited by the final product. In the first step, the 1D CuCl–thiourea template was readily produced when ethanolic solutions of CuCl, $SnCl_4$ and thiourea were vigorously stirred together. The resulting white gel mixture was then solvothermally heated at 160 °C for several hours, which facilitated the conversion of the sacrificial CuCl–thiourea nanotubes into the final Cu–Sn–S nanotubes. XRD analysis revealed that the resultant nanotubes are actually a mixture of Cu_2SnS_3, Cu_3SnS_4 and Cu_4SnS_4. With further examination, it was found that Cu_3SnS_4 and Cu_4SnS_4 co-exist in the inner walls of the tubes whereas Cu_2SnS_3 are primarily present on the rough-textured nanotube surface. Meanwhile, Ai et al. have employed a rapid

microwave-assisted synthetic strategy in the preparation of Cu_2FeSnS_4 nanotubes from *in situ* generated CuCl–thiourea nanorods.[98] Although a different heating technique is employed, the formation process is somewhat similar to that described above. First, CuCl–thiourea nanorods were precipitated out as white solids by vigorous mixing of thiourea and the metal chloride salts in benzyl alcohol at room temperature. These micrometer-long 1D structures initially exhibited smooth surface texture. However, after microwave irradiation at 180 °C for 1 s, the template exterior became rough as tiny Cu_2FeSnS_4 nanocrystals nucleated on the surface. With further microwave heating, the sacrificial nanorods gradually disappeared as they are transformed into tubular Cu_2FeSnS_4 nanostructures with mesoporous surface and hollow interiors. The length and diameter of the resultant nanotubes are similar to those of the sacrificial nanorods.

Wu and co-workers have shown that pre-synthesized micron-sized spheres of binary CuS can serve as a sacrificial hard template for porous architectures of ternary $CuInS_2$.[99] Figure 4c shows that the final morphology of the desired ternary material varies depending on the morphology of the starting binary CuS template. Basically, a hollow CuS template would yield a hollow $CuInS_2$ product in the same way that its non-hollow counterpart would give non-hollow $CuInS_2$. However, in both cases, there is a marked difference in the surface texture between the template and the product. As one can see in the TEM images in Figure 4c, the templates exhibit a relatively smoother exterior while the products possess a flakier surface. This is because $CuInS_2$ nanoflakes are initially formed at the template surface. Under solvothermal conditions, indium ions in solution react with the surface atoms of the extremely insoluble CuS template to produce $CuInS_2$ nanoflakes on the surface. With continued solvothermal heating, the conversion of the CuS template gradually extends from the surface toward the inner regions, and continues until complete transformation to $CuInS_2$ is achieved. Porous architectures of binary copper sulfide materials are convenient sacrificial hard

templates for porous copper-based ternary sulfide nanostructures because the transformation would merely involve the incorporation of an additional element. In a similar manner, porous nanostructures of copper-based ternary sulfides can be suitably utilized as structural frameworks for the construction of porous copper-based quaternary sulfide nanomaterials. As an example, Dong et al. have used the hollow Cu_2GeS_3 nanocrystals that they have created through the Kirkendall-type hollowing process as template materials for hollow nanocrystals of quaternary Cu_2MGeS_4, where M = Zn, Ni, Co, Fe and Mn.[64] The procedure simply involves the rapid injection of a solution of the M precursor into a hot dispersion of the hollow Cu_2GeS_3 nanocrystals. During the reaction, the divalent M ions gradually diffuse into the hollow Cu_2GeS_3 template, consequently converting it into the corresponding quaternary material.

Combining hard-templating with the Kirkendall diffusion process can be instrumental in realizing porous CMS nanostructures with unique architectures. This has been demonstrated by Zai et al. in their construction of cubic $CuInS_2$ nanocages from Cu_2O nanocubes.[100] In the first stage of the solvothermal reaction, indium and sulfur ions in solution react with surface copper ions of the pre-made Cu_2O cubic template, generating a layer of $CuInS_2$ on the template surface. This is followed by a Kirkendall-type hollowing process, in which the migration of Cu^+ from the nanocube interior is faster than the inward migration of In^{3+} and S^{2-}. As Cu^+ ions are exhausted from the Cu_2O core, the oxide ions that are left behind react with H^+ in solution to form H_2O. Finally, hollow $CuInS_2$ nanocubes (i.e., nanocages) are obtained. Although a hollow interior exists in the final product, the over-all cubic geometry of the template is preserved.

2.3.2. Soft templates

The soft-templating approach makes use of fluid templates in directing the formation of porous architectures.[41–43] After the final porous structures are generated, the soft templates often disappear

on their own or are removed by thoroughly washing the solid product with appropriate solvents. Vesicles (or micelles) are soft templates that are formed in solution when amphiphilic molecules self-assemble into well-defined structures from which hollow architectures can be moulded. In their synthesis of hollow $CuInS_2$ microspheres, Zhang et al. have proposed a vesicle-template-mediated mechanism to explain the formation of a hollow interior in their final product.[101] A pictorial representation of the formation process is displayed in Figure 5a. First, vesicles are generated from self-assembly of the cationic surfactant molecules, cetyltrimethylammonium bromide (CTAB), when heated at 80 °C in ethylene glycol. There are two types of vesicle structures that are created: (1) spherical vesicle (denoted as vesicle A in the scheme) and (2) peanut-like vesicle (vesicle B), which may be viewed as a combination of two or more spherical vesicles. Because of the cationic surface of the CTAB vesicles, the sulfide ions in solution are electrostatically attracted to the vesicle surface. Thus, when copper and indium ions are introduced in the reaction mixture, nucleation of $CuInS_2$ occurs at the template surface where the sulfide ions are situated. As the reaction continues, an amorphous layer of $CuInS_2$ is formed around the template surface, and this amorphous shell becomes crystalline in the subsequent refluxing process. In the final step, the vesicle template is extracted through washing, leaving behind hollow $CuInS_2$ spheres and peanut-like $CuInS_2$ architectures. A representative TEM image of the final product is included in Figure 5a.

Chelating agents, polymers, and gas bubbles can also be utilized as soft templates for the fabrication of hollow CMS architectures. For instance, the use of the disodium salt of ethylenediaminetetraacetic acid (EDTA) as a chelating soft template has been demonstrated by Zhang and co-workers in their hydrothermal synthesis of hollow Cu_2SnS_3 microspheres.[102] As a chelating agent, EDTA is able to coordinate to the copper and tin ions, and this facilitates the formation of a Cu_2SnS_3 layer on the surface of the EDTA template. Polycrystalline hollow Cu_2SnS_3

microspheres are obtained after several hours of hydrothermal heating, and the template is removed by washing the solid product thoroughly with water and ethanol. Meanwhile, Qu et. al have fabricated hollow Cu_2SnS_3 microspheres using a polymeric material, polyethylene glycol (PEG), as the soft template.[103] PEG can self-organize into mesoporous spheres under solvothermal conditions, and these spherical PEG structures can act as nucleation sites for the reaction between the metal ions and the sulfide anions. In a paper by You et al., a bubble template mechanism was proposed to describe the formation of their hierarchical $CuCo_2S_4$ hollow spheres, the schematic depiction of which is displayed in Figure 5b.[104] The bubble templates are believed to be NH_3 and H_2S gas bubbles that are generated *in situ* from the decomposition of thiourea molecules during the solvothermal process. The gas–liquid interface between the bubbles and the solvent provides adsorption sites where primary $CuCo_2S_4$ nanoparticles aggregate and ultimately grow into hierarchical hollow spheres. It was noted that when sulfur powder was used instead of thiourea as the sulfur source, no gas bubbles are released and thus the interiors of the final structures in this case are non-hollow. The bubble-templating approach has also been reported by Ramasamy et al. in the formation of hollow Cu_2GeS_3 nanostructures.[105] In their work, the hot-injection technique was employed where the thiol precursors are rapidly injected into a hot oleylamine dispersion of the copper and germanium precursors. The decomposition of thiols spawned the H_2S gas bubbles that served as aggregation centers for the eventual formation of Cu_2GeS_3 nanocrystals having hollow interiors.

Cha et al. have reported a sacrificial soft-templating process where Ga droplets are employed as a reactive fluid template for the fabrication of hollow $CuGaS_2$ spheres.[106] Figure 5c shows the schematic illustration of the proposed formation mechanism. Note that elemental Ga exists in liquid form at temperatures above 29.7 °C. In the first step, a dispersion of Ga metal in ethylene glycol is

prepared through sonochemical treatment. The ultrasound energy breaks up the liquid Ga metal into smaller spheres (i.e., droplets), which transitions into solid Ga nanospheres when the liquid mixture is cooled below the melting point of Ga. When copper and sulfur precursors are introduced in the reaction mixture under ultrasonication at 90 °C, a layer of CuS is deposited onto the surface of the Ga nanospheres. The resulting Ga–CuS core–shell spherical structures are then transformed into hollow $CuGaS_2$ spheres through thermal annealing at 450 °C under sulfidizing conditions. Because of the very high temperature, the low-melting Ga core rapidly diffuses into the CuS shell and leaves behind a central void in a manner reminiscent of the Kirkendall cavitation process.

3. Properties and Applications

CMS nanostructures are well recognized for their great potential in a variety of energy conversion domains. With the incorporation of porosity, they become endowed with new and improved properties that can be exploited for use in a wider scope of applications. In this section, we highlight their potential utility in the areas of biomedicine, energy storage, catalysis and sensing.

3.1 Biomedicine

In the biomedical field, pore-containing nanostructures are prime candidates as drug delivery vehicles.[51–54] Their porous morphological features are able to provide empty spaces that are large enough for drug molecules to penetrate, and their large surface area can be functionalized with suitable capping agents such that the release of drugs can be regulated under specific conditions. With the drug molecules encapsulated into the pores, they are safeguarded from immediate reaction or degradation in physiological environments prior to their release, and they can be made to selectively target the diseased cells, thereby avoiding possible adverse effects to healthy cells. When evaluating nanomaterials for biomedical usage, multifunctionality is often sought after. For example, it is highly desirable that drug nanocarriers possess additional favorable

properties aside from their drug loading capabilities. Recently, nanomaterials that display ability for photothermal (or light-to-heat) conversion are garnering considerable attention in the biomedical industry because the heat generated by light stimulation can be effectively used in killing cancerous cells through hyperthermia.[107,108] Particular interest is given to materials that can strongly absorb light in the near-infrared (NIR) spectral window as this low-energy light is minimally absorbed by biological tissue components and is less damaging to healthy tissues. When NIR-light-responsive nanostructures are made porous, a dual-modal therapeutic system that is capable of both photothermal tumor ablation and controlled drug delivery is realized. The combined effects of photothermal therapy and chemotherapy could then lead to enhanced treatment efficacy.

Nanostructures of noble metals (e.g. Au, Pd) are the most extensively explored photothermal agents owing to their tunable surface plasmon resonance (SPR), but their practical utility is limited by their high cost and non-biodegradability.[107–110] In recent years, NIR-absorbing copper sulfides (e.g. CuS, Cu_9S_5) have proven to be promising alternatives to noble metals due to their low cost, biodegradability, low cytotoxicity, high photostability and high photothermal conversion efficiency.[40,111–114] Like their parent binary copper sulfides, a number of CMS compounds have been found to absorb strongly in the NIR region. In previous studies of the photothermal properties of copper sulfide nanostructures, it was revealed that porous hierarchical architectures (e.g. flower-like structures) can effectively promote NIR light absorption because they behave as good laser-cavity mirrors.[114] This observation has also been noted in a paper by Wu et al., where the cavity-mirror effect is believed to contribute substantially to the intense NIR absorption of their porous $CuInS_2$ microspheres.[99] In this so-called cavity-mirror effect, porous architectures can trap NIR photons that enter their cavities upon laser irradiation. The trapped

photons are reflected several times within the cavities until they are eventually absorbed, resulting in significantly improved light absorption. The more photons are absorbed, the greater the amount of heat generated, and thus a porous architecture could facilitate a more impactful photothermal effect.

The possible use of multiply-voided $Cu_{12}Sb_4S_{13}$ nanotetrahedrons as a photothermally active drug delivery agent has been investigated recently.[89] After surface functionalization with 3-mercaptopropionic acid (MPA), the porous nanotetrahedrons are rendered water-dispersible and could be loaded with the anti-cancer drug, doxorubicin hydrochloride (DOX). It was found that the MPA-capped porous nanotetrahedrons exhibit a sustained and pH-sensitive drug release behavior, in which DOX is preferably released under acidic conditions. This is desirable in cancer therapy because cancerous cells thrive in acidic environments. Moreover, because the porous $Cu_{12}Sb_4S_{13}$ nanotetrahedrons are NIR-light-absorbers and are capable of photothermal conversion (left panel in Figure 6), the release of DOX from these nanocarriers can be regulated further through NIR-light-induced heating. The right panel in Figure 6 shows that the DOX release rate can be markedly accelerated when the nanotetrahedrons are irradiated with 808-nm light (i.e, ON mode). Triggered drug delivery systems such as these porous $Cu_{12}Sb_4S_{13}$ nanotetrahedrons can be suitably used as smart drug carriers as they allow for targeted delivery and controlled release of therapeutics.

Through a combinatorial therapeutics approach, Zhou and co-workers have shown that their PEG-coated (PEG = polyethylene glycol) Cu_3BiS_3 hollow nanostructures, which display good DOX-loading capacity and NIR-light responsiveness, are able to obliterate cancerous cells.[115] Figure 7 shows the hematoxylin–eosin stained histological images of tumor tissues from melanoma-inflicted mice treated under different conditions. With the tumor-bearing mice

injected with only PBS (phosphate-buffered saline) taken as control, a significant number of necrotic cells was seen in mice injected with DOX-loaded Cu_3BiS_3 hollow nanostructures (i.e., chemotherapy only) and in those injected with non-loaded Cu_3BiS_3 hollow nanostructures followed by laser irradiation (i.e., photothermal therapy only). While individual use of chemotherapy and phototheraphy is successful in destroying tumor cells, the largest number of tumor cell deaths was observed in mice treated with DOX-loaded Cu_3BiS_3 hollow nanostructures followed by laser irradiation (i.e., combined chemo- and photothermal therapy). This clearly proves that the synergistic action of DOX and hyperthermia can bring about a remarkable enhancement in treatment efficacy.

An advantage of using Cu_3BiS_3 over binary copper sulfides is that it can also serve as a contrast agent for X-ray computed tomography (CT) imaging owing to the large X-ray attenuation coefficient of Bi. Aside from their therapeutic properties, the Cu_3BiS_3 hollow nanostructures displayed good CT imaging capability when tested on tumor-bearing mice.[115] Similarly, a recent report by Yu et al. has shown that urchin-shaped nanocomposites having Cu_3BiS_3 cores can function as both photothermal and CT contrast agents.[116] Thus, with the added imaging functionality, porous Cu_3BiS_3 nanostructures can be both therapeutic and diagnostic agents making them ideal for cancer theranostics.

3.2 Energy storage

Porous nanomaterials have been extensively explored for energy storage applications.[36,42,43,55–59,117] Their large surface area and porous architecture can provide several advantages in the development of promising electrode materials for rechargeable batteries and supercapacitors. First, the large surface area leads to increased electrode–electrolyte interface that is highly favorable for electron and ion transport, and the nanosize domains of porous materials can

provide shorter ion diffusion pathways. Moreover, the porous morphology can accommodate the volumetric expansion of electrodes during charge-discharge cycling with the aim of preserving the integrity of the structure. The porous structure can also offer richer redox reaction active sites, leading to higher capacity/capacitance. Thus, porosity has been incorporated in a large variety of suitable electrode materials for energy storage, which include silicon,[118] carbon,[119] metal oxides,[120–121] and their composites (e.g. Fe_3O_4/C, C/MnO_2, Si/C).[122–124] With its very high theoretical capacity (4200 mAh g^{-1}) and long cyclic lifetimes, silicon displays enormous potential as electrode materials in lithium-ion storage. However, only a small portion of the theoretical capacity is typically reached (e.g. only 35.7% capacity utilization was reported for some carbon-coated porous silicon anodes),[124,125] and practical application is largely hampered by the high cost of producing nanostructured Si with porous features.[118] Porous carbon-based electrodes are relatively less costly to prepare, and the specific capacity can reach the theoretical value of 372 mAh g^{-1},[126] but they are generally limited by their low theoretical capacity. In recent years, metal sulfides are attracting increasing attention in the field of energy storage due to their high specific capacity, which are two to three times higher than those of carbon-based materials.[127,128] They have also shown better electrochemical performance than metal oxides, which suffer from poor electronic conductivity.[129] Multinary metal sulfides such as the CMS compounds are superior to binary metal sulfides because they possess richer redox chemistry and higher electronic conductivity. Moreover, by tuning the composition of the multinary sulfide materials, suitable electrochemical potentials and properties can be obtained.

Ternary Cu_2SnS_3 is one of the most often studied CMS compounds in the field of lithium-ion storage. Numerous groups have evaluated the use of porous Cu_2SnS_3 as anode materials in lithium-ion batteries. The discharge-charge cycling curves of Li/Cu_2SnS_3 cells assembled with hollow

Cu_2SnS_3 microspheres[102] and mesoporous Cu_2SnS_3 microspheres[103] show high initial lithiation capacities of 1316 and 891 mAh g^{-1}, respectively, at a current density of 100 mA g^{-1}. However, both decay rapidly to about 300 and 378 mAh g^{-1}, respectively, after 22 cycles. Zhang et al. noted that the large capacity loss could be attributed to the formation of insulating Li_2S onto the surface of the electrode materials, which is typically observed in metal sulfide-based electrodes.[102] Meanwhile, anode materials based on hierarchical cabbage-like architectures of Cu_2SnS_3 have been demonstrated to deliver an initial reversible capacity as high as 842 mAh g^{-1}, with only 17.5% initial capacity loss and above 61% capacity retention after 50 cycles at a current density of 100 mA g^{-1}.[130] Such remarkable performance is attributed to their 3D porous network structural features. In a more recent paper, Lin et al. have reported the influence of morphology and composition on the (de)lithiation performance of their porous Cu–Sn–S nanostructures.[97] They have compared the performance of three different samples: (1) composite nanotubes with $Cu_{3-4}SnS_4$ core and Cu_2SnS_3 shell, (2) composite sub-nanotubes with Cu_2SnS_3 core and $Cu_{3-4}SnS_4$ shell, and (3) Cu_2SnS_3 nanoparticles. Among them, the composite nanotubes were found to exhibit the best cycling performance and rate capability as shown in Figure 8. The ability of the porous tube structure to mitigate the volumetric expansion during cycling, as well as the presence of abundant Cu_4SnS_4 phase with improved lithiation properties in the composite nanotubes were found to play important roles in the enhancement of electrochemical performance.

Hollow $CuInS_2$ nanospheres have also been investigated for their potential application as an anode material for rechargeable lithium-ion batteries.[131] As compared to non-hollow $CuInS_2$ nanoparticles, the structurally more stable hollow $CuInS_2$ nanospheres have shown superior electrochemical performance. Meanwhile, nanostructured Cu_2ZnSnS_4 having flake-like surface and slit-like pores has been successfully utilized as a cathode material, where a high initial discharge

capacity of 1154 mAh g^{-1} and a small capacity decay were achieved (i.e., stabilized at about 680 mAh g^{-1} after 40 cycles at a current rate of 100 mA g^{-1}).[132] The potential of hierarchical Cu_3BiS_3 nanostructures as an anode and a cathode material for rechargeable lithium storage systems have been explored in separate studies. Zeng et al. showed that when applied as an anode material for Li-ion batteries, their flower-like Cu_3BiS_3 structures exhibited an initial discharge capacity of 676 mAh g^{-1} but it degraded quickly during subsequent cycles.[133] In another study, Gao et al. used Cu_3BiS_3 with similar flower-like structures as a host cathode material for lithium-sulfur batteries.[134] The discharge specific capacity of Cu_3BiS_3/S in the first cycle was measured to be 1343 mAh g^{-1} at a current rate of 0.2 C, but a gradual decrease to 487 mAh g^{-1} was observed after 100 cycles. Although the initial discharge specific capacity is comparable with those reported in current works for other types of porous materials,[135,136] the cycling stability requires much improvement, and so future efforts should focus on better encapsulating the sulfur-based cathodes to minimize polysulfide dissolution into the electrolyte and the resulting shuttle effect.

The use of flower-like Cu_2NiSnS_4 structures as anode materials for rechargeable sodium-ion batteries has been assessed by Yuan and co-workers.[77] A high initial discharge capacity of 631 mAh g^{-1} was obtained at a current density of 25 mAh g^{-1}, and this was further enhanced to 840 mAh g^{-1} by homogeneous integration with reduced graphene oxide (rGO) nanosheets. When compared with nanostructured Cu_2NiSnS_4 with irregular morphology, their performance is superior in terms of specific capacity, rate capability and cycling stability, owing to their 3D hierarchical architecture, which provides fast ion diffusion pathways and large contact area at the electrode–electrolyte interface.

Very recently, several groups have reported the supercapacitor application of $CuCo_2S_4$ nanomaterials with varying porous morphologies, such as mesoporous nanorod arrays, hollow

nanoneedle arrays and mesoporous nanoparticles.[137–139] When evaluated as electrode materials for supercapacitors, the different porous $CuCo_2S_4$ nanostructures all exhibited ultrahigh specific capacitance, high energy density, outstanding rate capability and excellent cycling stability. These exceptional supercapacitive properties can be attributed to: (1) the large surface area and permeability of the porous structure; (2) the high conductivity of multinary metal sulfides; and (3) the abundant reversible redox reactions of $Co^{4+}/Co^{3+}/Co^{2+}$ and Cu^{2+}/Cu^{+}. As displayed in Figure 9, the specific capacitance measured for the mesoporous $CuCo_2S_4$ nanorod array electrode can reach 1536.9 F g^{-1} at a current density of 1 A g^{-1}, and can maintain 1235.2 F g^{-1} after 10000 cycles.[137] These values are considerably larger than those obtained for mesoporous $CuCo_2O_4$ nanowire array electrode (also shown in Figure 9), and this can be attributed to the better electronic conductivity and stability of $CuCo_2S_4$ relative to its corresponding oxide compound. Using porous $CuCo_2S_4$ nanomaterials as the positive electrode and activated carbon as the negative electrode, high-performance asymmetric supercapacitor devices have been successfully fabricated.

3.3 Catalysis

CMS semiconductors are highly regarded materials in photocatalysis owing to their exceptional light-harvesting properties and easily tunable band structures. They possess certain advantages over other known classes of photocatalytic materials, such as stronger absorption in the visible spectrum compared to metal oxides (e.g. TiO_2, ZnO), and lower toxicity compared to cadmium chalcogenides (e.g. CdS).[1,9] When porosity is introduced, the photocatalytic properties can be greatly enhanced due to increased number of catalytically-active sites for guest molecules, lower diffusion barriers, improved mass transport and shorter diffusion pathways of the electron−hole pairs.[42,44] Porosity can also promote high light utilization efficiency due to the deep penetration of light through the channels, the multiple reflection of light within the cavities, as well as the long light pathway.

Hierarchical Cu_2SnS_3 flower-like structures[140] and mesoporous $CuInS_2$ spheres[141] have both been shown to exhibit superior photocatalytic activities for the degradation of organic dyes under visible-light irradiation, which can be credited to their porous structure, large surface area, and suitable band gap. The Cu_2SnS_3 flowers displayed effective catalysis for oxidative decomposition of methylene blue whereas the mesoporous $CuInS_2$ spheres exhibited catalytic behaviour in the degradation of Rhodamine B. Meanwhile, two groups have recently reported the enhanced photocatalytic performance of porous Cu_2MoS_4-based composites in the degradation of methyl orange.[142,143] The composites consist of Cu_2MoS_4 hollow nanostructures and reduced graphene oxide (rGO). The incorporation of rGO was found to promote stronger and wider absorption in the visible spectral range and to effectively suppress electron–hole recombination, leading to considerable enhancement in dye degradation efficiency compared to the pure Cu_2MoS_4 hollow nanostructures (e.g. 99% for the Cu_2MoS_4–rGO composite vs. 57% for pure Cu_2MoS_4 after 40 min of irradiation).[143] Therefore, by integrating large surface area with enhanced light absorption and better charge separation, greatly improved photocatalytic performance can be achieved.

Another means of boosting the photocatalytic performance of CMS materials is to manipulate their band structure via alloying.[8,9] This is perfectly exemplified by $(CuInS_2)_{1-x}(ZnS)_x$, a quaternary alloy of ternary $CuInS_2$ and binary ZnS. Note that ZnS has a wide band gap (E_g = 3.7 eV) that is not suited for visible-light absorption while $CuInS_2$ (E_g = 1.5 eV) has a conduction band minimum that is not high enough for reducing H_2O to H_2.[10] By adjusting the band structure through alloying, an optimal alloy composition with superior photocatalytic performance for hydrogen production is achieved. Two separate groups have reported the fabrication of a series of $(CuInS_2)_{1-x}(ZnS)_x$ samples having mesoporous 3D hierarchical structures for photocatalytic hydrogen generation.[81,82] Both groups observed the highest photocatalytic activity for $Cu_{0.2}Zn_{1.6}In_{0.2}S_2$ ($CuInS_2$/ZnS ratio of

1:8), implying that this alloy composition has the optimal band structure.

CMS compounds, such as Cu_2MoS_4 and Cu_2WS_4, are among the most attractive mixed metal sulfide materials that are currently being investigated as low-cost alternatives to Pt for electrocatalytic hydrogen evolution reaction (HER), owing to their excellent electrocatalytic activity over a wide pH range.[128,144] For instance, Zhang et al. have explored the usefulness of Cu_2MoS_4 nanostructures for HER and compared the catalytic properties of three different morphologies: hollow nanoflowers, nanosheets and nanoparticles.[145] As one can see in Figure 10, the hollow nanoflowers displayed an onset overpotential (165 mV) and a Tafel slope (64 mV dec^{-1}) that are significantly lower than those of the nanosheets (240 mV and 98 mV dec^{-1}) and the nanoparticles (175 mV and 71 mV dec^{-1}). These values are comparable to those recently reported for flower-like structures of the highly promising HER catalyst MoS_2 (i.e., 100 mV and 80.5 mV dec^{-1}).[146] The excellent catalytic HER activity of the Cu_2MoS_4 hollow nanoflowers is attributed to their 3D hierarchical structure, which not only exposes more potential reactive sites for the catalytic reaction, but also prevents the negative effects of particle aggregation. Moreover, the hollow nanoflowers showed the best stability among the three morphologies because of their robust hollow frame.

The potential utility of hollow Cu_2GeS_3 nanostructures as photoelectrode materials have been evaluated by Dong and co-workers.[65] A two-layer photoelectrode with both large and small hollow Cu_2GeS_3 nanostructures has been constructed to integrate the advantages of the two different sizes. The large hollow nanostructures with huge cavity not only increase the contact area between the active sites and electrolyte, but also expedite the formation of photogenerated carriers and reduce electron–hole recombination. The monodisperse small hollow nanostructures, on the other hand, form a dense and compact film to block the potential oxidation side reactions on the conductive substrate. As a result, the two-layer photoelectrode exhibits superior performance with substantially

higher photocurrent density than those of the photoelectrodes prepared with only large and only small Cu_2GeS_3 hollow nanostructures. This type of photoelectrode structural design could be useful in photoelectrocatalytic applications, not only for water splitting, but also for emerging reactions such as carbon dioxide reduction.[147,148]

3.4 Sensing

Sensitivity, cost and durability are primarily considered when selecting materials that can be incorporated as sensors in sensing devices. With the burgeoning popularity of CMS compounds in many important technologies, these materials are also starting to attract significant interest in sensing applications. The performance of sensing materials is known to depend crucially on their size and morphology. To achieve enhanced sensing properties, materials with nanometer-scale dimensions and porous morphologies are desirable due to their high surface-to-volume ratio, which equates to having a large number of available adsorption sites for target species.[41–43,47–50] Moreover, the permeability of a porous structure can promote diffusion and transport of analyte molecules, enabling contact of these molecules with more active surfaces.

The ethanol gas sensing properties of hollow and non-hollow Cu_2GeS_3 nanocrystals were compared by Dong et al. by examining their response toward 5 ppm ethanol gas under different operating temperatures.[64] Figure 11 shows that although the optimum operating temperatures are different for the two samples, the hollow structured-based sensors exhibited better sensitivity than their non-hollow counterparts under all operating temperatures. The response transient curves recorded under their optimum operating temperatures revealed that their response time and recovery time are the same, which indicates that they operate through a similar gas sensing mechanism. The sensing process is considered to be a space-charge region model that involves gas adsorption, charge transfer, and desorption steps. Based on the mechanism described, the

superior gas sensing performance displayed by the hollow Cu_2GeS_3 nanocrystals as compared to the non-hollow ones can be attributed to their higher surface-to-volume ratio and their smaller grain size. With the hollow morphological structure having both inner and outer specific surface area, its total surface area is larger and thus provides more active adsorption sites toward ethanol gas molecules. Meanwhile, small grain size is advantageous for the charge separation and transfer in the same space-charge region. When compared to porous structures of the more popular ethanol sensing material ZnO, the ethanol gas sensing performance of the hollow Cu_2GeS_3 nanostructure-based sensor is fairly similar in terms of the detection limit (as low as 5 ppm) and the optimal operating temperature (e.g. 230 °C for hollow Cu_2GeS_3 and 250 °C for dandelion-like ZnO).[49]

In a recent study by Yang et al., $CuCo_2S_4$ flower-like architectures with high surface-to-volume ratio have been found to exhibit exceptional electrochemical performance for non-enzymatic detection of H_2O_2.[149] The electrochemical sensing properties of the porous $CuCo_2S_4$-modified electrode were deemed remarkable in terms of linear range, sensitivity and detection limit. The sensitivity can be as high as 857.1 μA mM^{-1} cm^{-2}, while the detection limit can be as low as 0.084 μM. Moreover, a low amperometric response was observed after addition of interference agents, indicating good selectivity. The outstanding electrocatalytic activity observed toward H_2O_2 oxidation can be ascribed to the abundant redox active sites in this mixed-metal sulfide nanomaterial. The 3D tunnelled architecture can also provide abundant spaces and channels for the diffusion and transport of H_2O_2 molecules.

4. Summary and outlook

Porous nanostructures are attractive in both fundamental research and practical applications due to the excellent properties that arise as a result of their porous morphological features. When

combined with the intrinsic properties of technologically important materials like the CMS compounds, the numerous favorable characteristics afforded by a porous nanostructure morphology could bring about further enhancement of material properties and widen the range of their technological applications. With the multiple advantages that can be gained from porosity, increasing attention is targeted to the design and tailoring of porous nanostructures of a wide variety of functional materials.

In constructing porous nanostructures of CMS materials, several approaches have been developed on the basis of different pore formation principles, which define the type of porous morphology assumed by the final product. For instance, the Kirkendall-type hollowing approach operates through a vacancy-mediated diffusion mechanism where a central interior pore is generated within a nanocrystal due to the different diffusion rates of the elemental components. As a consequence, the final product are hollow nanocrystals with a single well-defined void at the core. An advantage of this approach is that it is possible to produce high-quality nanocrystals with controlled hollow interior by carefully manipulating the reaction conditions that influence the cavitation process, such as the reaction temperature and precursor reactivity. However, as unequal atomic diffusion plays a critical role in the hollowing mechanism, this mode of pore formation becomes progressively more challenging with increasing number of elemental components that must come together to form the desired multinary compound. This may be the reason why hollow nanocrystals of more complex CMS compositions have not yet been produced through this method. Meanwhile, in the aggregation-based pore formation mode, void spaces are conveniently created during the lumping together of nanoscale building blocks and this renders porosity to the final 3D structure. The porous structures that are produced from this aggregative growth process are typically large and multiply-voided. This simple pore-forming strategy has been used to fabricate

mesoporous structures of a vast range of CMS compositions, including a series of quaternary alloys. The multiple pores and the hierarchical tunnelled or layered structures that are created benefit many applications but precise control of pore qualities (e.g. size, distribution) has been difficult to achieve because the nanoscale components (e.g. the nanoflakes in flower-like structures) are often randomly arranged. Template-directed pore engineering is another effective means of constructing porous CMS nanostructures. The resultant porous structures typically exhibit hollow interiors and multiply-voided exteriors because the mode of growth is often through particle aggregation on the template surface or on the template pore walls. When hard templates (e.g. AAO) are used, it is possible to achieve uniform pore size distribution and unique shapes because these properties are inherited from the chosen templates. However, there is a need for an additional processing step for template removal except in the case of sacrificial hard templates, where the pre-formed templates are converted into the final porous product. For soft-templating, the templates disappear on their own or can be easily extracted by washing, but controlling the pore qualities can be a challenge because of the non-rigid structure of fluid templates (e.g. bubbles, vesicles).

The ability to create porous CMS nanostructures has inspired several groups to explore their use in applications where the unique features (e.g. large and accessible surface area) that result from porosity are desirable. In biomedicine, the excellent drug loading efficiency provided by porosity coupled with the intense NIR absorption inherent to CMS compounds allows for a bimodal cancer treatment (i.e., combined chemo- and photothermal therapy) with enhanced efficacy. In the case of Cu_3BiS_3, X-ray CT imaging is also possible due to the X-ray attenuation properties of Bi, making porous Cu_3BiS_3 nanostructures ideal for cancer theranostics. Apart from Cu_3BiS_3, there are other NIR-absorbing CMS compounds that show great potential for imaging and so future works should focus on exploring porous nanostructures of these materials for

theranostics. For example, $CuCo_2S_4$ nanocrystals were recently reported to display magnetic resonance (MR) imaging capability due to the magnetic characteristic of Co, in addition to having photothermal, infrared (IR) imaging and photoacoustic (PA) imaging properties.[150,151] We believe that incorporating porosity in $CuCo_2S_4$ would facilitate a more impactful photothermal effect and also bestow it with good drug loading capability for a more effective cancer treatment. Porosity could undoubtedly offer substantial opportunities to integrate different theranostic modalities into a single platform for combinatorial cancer therapy with real-time diagnosis.

The utility of porous CMS nanostructures in the areas of energy storage and catalysis have been increasingly studied over the past decade. Despite their promising performance in these fields, there are important issues that need to be overcome in order to meet the demands of real-world applications. As electrode materials for lithium storage applications, porous CMS nanostructures have shown high specific capacity but their long-term cycling stability has been less satisfactory. To address this issue, future research should be directed toward understanding the failure mechanisms upon cycling. By getting to the root of the problem, critical insights into the rational design of novel structures or composites can be gained. In photocatalysis, metal sulfides in general are faced with stability issues that arise from hole-induced oxidative photocorrosion.[152] Further efforts are needed to resolve this problem, such as finding suitable and inexpensive protective materials that can be easily integrated into the design of a photocorrosion-resistant composite photocatalyst. Meanwhile, the use of porous CMS nanostructures for sensing applications is still in its infancy. The very few known examples in the literature (e.g. ethanol gas sensing, electrochemical detection of H_2O_2) showed encouraging results and should inspire more scientists to conduct further research in this area.

Surprisingly, although CMS materials are best known for their use in the fields of energy

conversion (e.g. thermoelectrics and photovoltaics), detailed studies on the impact of porosity on their performance in these fields are lacking. In thermoelectrics, CMS compounds are deemed promising due to their complex crystal structures that give rise to low lattice thermal conductivity (k_L) and high figure-of-merit (ZT). In fact, remarkable ZT values have already been realized for bulk materials based on $Cu_{12}Sb_4S_{13}$ (e.g. ZT = 1.13 at 575 K for the Mn-substituted compound, $Cu_{11}MnSb_4S_{13}$) and Cu_5FeS_4 (e.g. ZT = 0.79 at 550 K).[153–155] However, the thermoelectric properties of porous nanostructures of these materials have not yet been examined. Recent works have shown that high porosity can considerably enhance phonon scattering and this can lead to ultralow k_L.[156,157] For example, porous nanocomposites based on $Bi_2Te_{2.5}Se_{0.5}$ hollow nanorods have shown extremely low k_L leading to a high ZT value of 1.18 at 463 K.[157] In addition to their outstanding performance, these highly porous thermoelectric nanomaterials have low density (i.e, lightweight) and this opens opportunities for their use in portable devices. With this exciting news about the power of pores in thermoelectrics, it is highly likely that the thermoelectric performance of porous nanomaterials based on $Cu_{12}Sb_4S_{13}$, Cu_5FeS_4 and some other CMS compounds can rival the best-performing Bi_2Te_3-based thermoelectric materials. Thus, we believe that the thermoelectric properties of porous CMS nanomaterials deserve to be given significant attention. Meanwhile, in photovoltaics, CMS compounds are ideally suited as absorber materials due to their excellent solar-harvesting properties. High solar cell conversion efficiencies have already been achieved by solid-state solar cells where thin films based on Cu_2ZnSnS_4 and $CuIn_xGa_{1-x}S_2$ serve as absorber layers.[11,158] Because most CMS materials are p-type semiconductors, an emerging direction is their incorporation as photocathodes in photoelectrochemical solar cells, such as dye-sensitized solar cells (DSSCs).[159,160] Porous nanostructures of CMS are particularly attractive in this regard due to the large surface area and improved light scattering effect that results from porosity. In DSSCs, the

porosity of the electrode material greatly influences the properties and efficiency of the device; hence, fine-tuning the pore qualities of CMS nanostructures and investigating the effect of these factors on solar cell performance must be dealt with in future studies.

Over the next several years, it is anticipated that research on porous CMS nanostructures will continue to flourish considering the tremendous opportunities that lie ahead for potential technological applications. Aside from CMS compounds, there are countless other interesting multinary compounds of which porous nanostructures have yet to be reported. Although significant progress has been made in the synthesis of porous multinary compound nanostructures, it has yet to advance to a level comparable to the synthesis of porous nanostructures of materials with simpler compositions. More sophisticated porous architectures and precise control of pore qualities have already been demonstrated for a wide array of metals and binary compounds.[36,41,161,162] The ability to control the porosity of materials could allow us to manipulate and refine their properties and cater them according to the needs of our fast-changing world. While multinary compositions allow for vaster structural and compositional diversity that can be tuned to suit desired applications, there is a higher degree of complexity in the synthesis of their porous nanostructures due to their multiple elemental constituents. Thus, the foremost challenge will be the development of advanced synthetic methods that could enable the construction of elaborate and tunable porous structures of a large number of technologically applicable multinary materials. This would require better understanding of pore formation processes, which could vary depending on material composition. Needless to say, more efforts should be dedicated to expanding our mechanistic understanding of pore formation. Lastly, issues concerning manufacturing cost and adaptability of methods for large-scale production have to be addressed before commercialization can be realized.

AUTHOR INFORMATION

Corresponding Author

*regulaciomdc@imre.a-star.edu.sg

Author Contributions

The manuscript was written through contributions of all authors. All authors have given approval to the final version of the manuscript.

Acknowledgements

This work was supported by the A*STAR SERC Pharos Programme (Grant Number: 1527200023) and the Singapore National Research Foundation (NRF-NRFF2017-04).

References

(1) C. Coughlan, M. Ibáñez, O. Dobrozhan, A. Singh, A. Cabot and K. M. Ryan. Compound Copper Chalcogenide Nanocrystals. *Chem. Rev.*, **2017**, *117*, 5865−6109.

(2) S. Sun, P. Li, S. Liang and Z. Yang. Diversified copper sulfide ($Cu_{2-x}S$) micro-/nanostructures: a comprehensive review on synthesis, modifications and applications. *Nanoscale*, **2017**, *9*, 11357−11404.

(3) P. Roy and S. K. Srivastava. Nanostructured copper sulfides: synthesis, properties and applications. *CrystEngComm*, **2015**, *17*, 7801−7815.

(4) Y. Liu, M. Liu and M. T. Swihart. Plasmonic Copper Sulfide-Based Materials: A Brief Introduction to Their Synthesis, Doping, Alloying, and Applications. *J. Phys. Chem. C*, **2017**, *121*, 13435−13447.

(5) Y.-K. Kim, S.-H. Ahn, K. Chung, Y.-S. Cho and C.-J. Choi. The photoluminescence of $CuInS_2$ nanocrystals: effect of non-stoichiometry and surface modification. *J. Mater. Chem.*, **2012**, *22*, 1516−1520.

(6) B. Chen, H. Zhong, W. Zhang, Z. Tan, Y. Li , C. Yu, T. Zhai, Y. Bando, S. Yang and B. Zou. Highly Emissive and Color-Tunable $CuInS_2$-Based Colloidal Semiconductor Nanocrystals: Off-Stoichiometry Effects and Improved Electroluminescence Performance. *Adv. Funct. Mater.*, **2012**, *22*, 2081−2088.

(7) O. Yarema, M. Yarema and V. Wood. Tuning the Composition of Multicomponent Semiconductor Nanocrystals: The Case of I−III−VI Materials. *Chem. Mater.*, **2018**, *30*, 1446−146.

(8) C. Ye, M. D. Regulacio, S. H. Lim, Q.-H. Xu and M.-Y. Han. Alloyed $(ZnS)_x(CuInS_2)_{1-x}$ Semiconductor Nanorods: Synthesis, Bandgap Tuning and Photocatalytic Properties. *Chem. Eur. J.*, **2012**, *18*, 11258–11263.
(9) M. D. Regulacio and M.-Y. Han. Multinary I–III–VI_2 and I_2–II–IV–VI_4 Semiconductor Nanostructures for Photocatalytic Applications. *Acc. Chem. Res.*, **2016**, *49*, 511–519.
(10) C. Ye, M. D. Regulacio, S. H. Lim, S. Li, Q.-H. Xu and M.-Y. Han. Alloyed ZnS–$CuInS_2$ Semiconductor Nanorods and Their Nanoscale Heterostructures for Visible-Light-Driven Photocatalytic Hydrogen Generation. *Chem. Eur. J.*, **2015**, *21*, 9514–9519.
(11) F.-J. Fan, L. Wu and S.-H. Yu. Energetic I–III–VI_2 and I_2–II–IV–VI_4 nanocrystals: synthesis, photovoltaic and thermoelectric applications. *Energy Environ. Sci.*, **2014**, *7*, 190–208.
(12) G. M. Ford, Q. Guo, R. Agrawal and H. W. Hillhouse. Earth Abundant Element $Cu_2Zn(Sn_{1-x}Ge_x)S_4$ Nanocrystals for Tunable Band Gap Solar Cells: 6.8% Efficient Device Fabrication. *Chem. Mater.*, **2011**, *23*, 2626–2629.
(13) S.-Y. Wei, Y.-C. Liao, C.-H. Hsu, C.-H. Cai, W.-C. Huang, M.-C. Huang and C.-H. Lai. Achieving high efficiency $Cu_2ZnSn(S,Se)_4$ solar cells by non-toxic aqueous ink: Defect analysis and electrical modeling. *NanoEnergy*, **2016**, *26*, 74–82.
(14) D. Aldakov, A. Lefrançois and P. Reiss. Ternary and quaternary metal chalcogenide nanocrystals: synthesis, properties and applications. *J. Mater. Chem. C*, **2013**, *1*, 3756–3776.
(15) X. Shen, E. A. Hernandez-Pagan, W. Zhou, Y. S. Puzyrev, J. C. Idrobo, J. E. Macdonald, S. J. Pennycook and S. T. Pantelides. Interlaced crystals having a perfect Bravais lattice and complex chemical order revealed by real-space crystallography. *Nat. Commun.*, **2014**, *5*, 5431.
(16) W. van der Stam, A. C. Berends and C. de Mello Donega. Prospects of Colloidal Copper Chalcogenide Nanocrystals. *ChemPhysChem*, **2016**, *17*, 559–581.
(17) S. Ananthakumar, J. Ram Kumar and S. Moorthy Babu. Evolution of non-phosphine solvents in colloidal synthesis of I–III–VI_2 and I_2–II–IV–VI_4 group semiconductor nanomaterials – Current status. *Mater. Sci. Semicond. Process.*, **2017**, *67*, 152–174.
(18) M. D. Regulacio, C. Ye, S. H. Lim, Y. Zheng, Q.-H. Xu and M.-Y. Han. Facile noninjection synthesis and photocatalytic properties of wurtzite-phase $CuGaS_2$ nanocrystals with elongated morphologies. *CrystEngComm*, **2013**, *15*, 5214–5217.
(19) M. D. Regulacio, C. Ye, S. H. Lim, M. Bosman, E. Ye, S. Chen, Q.-H. Xu and M.-Y. Han. *Chem. Eur. J.*, **2012**, *18*, 3127–3131.
(20) K. Chen, J. Zhou, W. Chen, Q. Zhong, T. Yang, X. Yang, C. Deng and Y. Liu. Growth kinetics and mechanisms of multinary copper-based metal sulfide nanocrystals. *Nanoscale*, **2017**, *9*, 12470–12478.
(21) B. Chen, N. Pradhan and H. Zhong. From Large-Scale Synthesis to Lighting Device Applications of Ternary I−III−VI Semiconductor Nanocrystals: Inspiring Greener Material Emitters. *J. Phys. Chem. Lett.*, **2018**, *9*, 435–445.
(22) S. Liu and X. Su. The synthesis and application of I–III–VI type quantum dots. *RSC Adv.*, **2014**, *4*, 43415–43428.
(23) M. D. Regulacio and M.-Y. Han. Composition-Tunable Alloyed Semiconductor Nanocrystals. *Acc. Chem. Res.*, **2010**, *43*, 621–630.

(24) Y. Sun, B. Mayers and Y. Xia. Metal Nanostructures with Hollow Interiors. *Adv. Mater.*, **2003**, *15*, 641–646.
(25) Y. Yin, C. K. Erdonmez, A. Cabot, S. Hughes and A. P. Alivisatos. Colloidal Synthesis of Hollow Cobalt Sulfide Nanocrystals. *Adv. Funct. Mater.*, **2006**, *16*, 1389–1399.
(26) A.-A. El Mel, R. Nakamura and C. Bittencourt. The Kirkendall effect and nanoscience: hollow nanospheres and nanotubes. *Beilstein J. Nanotechnol.*, **2015**, *6*, 1348–1361.
(27) H. Tianou, W. Wang, X. Yang, Z. Cao, Q. Kuang, Z. Wang, Z. Shan, M. Jin and Y. Yin. Inflating hollow nanocrystals through a repeated Kirkendall cavitation process. *Nat. Commun.*, **2017**, *8*, 1261.
(28) Y. Xiong, B. Wiley, J. Chen, Z.-Y. Li, Y. Yin and Y. Xia. Corrosion-Based Synthesis of Single-Crystal Pd Nanoboxes and Nanocages and Their Surface Plasmon Properties. *Angew. Chem. Int. Ed.*, **2005**, *44*, 7913–7917.
(29) J. Chen, B. Wiley, J. McLellan, Y. Xiong, Z.-Y. Li and Y. Xia. Optical Properties of Pd−Ag and Pt−Ag Nanoboxes Synthesized via Galvanic Replacement Reactions. *Nano Lett.*, **2005**, *5*, 2058–2062.
(30) A. Genç, J. Patarroyo, J. Sancho-Parramon, N. G. Bastús, V. Puntes and J. Arbiol. Hollow metal nanostructures for enhanced plasmonics: synthesis, local plasmonic properties and applications. *Nanophotonics*, **2017**, *6*, 193–213.
(31) Z. Cheng, S. Wang, Q. Wang and B. Geng. A facile solution chemical route to self-assembly of CuS ball-flowers and their application as an efficient photocatalyst. *CrystEngComm*, **2010**, *12*, 144–149.
(32) X. Sun, S. Xu, Y. Gao, M. Yue, Q. Yue and B. Gao. 3D hierarchical golden wattle-like TiO_2 microspheres: polar acetone-based solvothermal synthesis and enhanced water purification performance. *CrystEngComm*, **2017**, *19*, 2187–2194.
(33) C.-M. Lan, S.-E. Liu, J.-W. Shiu, J.-Y. Hu, M.-H. Lin and E. W.-G. Diau. Formation of size-tunable dandelion-like hierarchical rutile titania nanospheres for dye-sensitized solar cells. *RSC Adv.*, **2013**, *3*, 559–565.
(34) J. Zhao, Y. Liu, M. Fan, L. Yuan and X. Zou. From solid-state metal alkoxides to nanostructured oxides: a precursor-directed synthetic route to functional inorganic nanomaterials. *Inorg. Chem. Front.*, **2015**, *2*, 198–212.
(35) M.-H. Sun, S.-Z. Huang, L.-H. Chen, Y. Li, X.-Y. Yang, Z.-Y. Yuan and B.-L. Su. Applications of hierarchically structured porous materials from energy storage and conversion, catalysis, photocatalysis, adsorption, separation, and sensing to biomedicine. *Chem. Soc. Rev.*, **2016**, *45*, 3479–3563.
(36) L. Yu, H. Hu, H. B. Wu and X. W. Lou. Complex Hollow Nanostructures: Synthesis and Energy-Related Applications. *Adv. Mater.*, **2017**, *29*, 1604563.
(37) Q. Lu and F. Gao. Synthesis and property studies of hollow nanostructures. *CrystEngComm*, **2016**, *18*, 7399–7409.
(38) H. Sun, X. Xu, Z. Yan, X. Chen, F. Cheng, P. S. Weiss and J. Chen. Porous Multishelled Ni_2P Hollow Microspheres as an Active Electrocatalyst for Hydrogen and Oxygen Evolution. *Chem. Mater.*, **2017**, *29*, 8539−8547.
(39) Q. Zhang, W. Wang, J. Goebl and Y. Yin. Self-templated synthesis of hollow nanostructures. *Nano Today*, **2009**, *4*, 494–507.
(40) L. Han, Y.-N. Hao, X. Wei, X.-W. Chen, Y. Shu and J.-H. Wang. Hollow Copper Sulfide Nanosphere−Doxorubicin/Graphene Oxide Core−Shell Nanocomposite for Photothermo-chemotherapy. *ACS Biomater. Sci. Eng.*, **2017**, *3*, 3230−3235.

(41) C. Zhu, D. Du, A. Eychmüller and Y. Lin. Engineering Ordered and Nonordered Porous Noble Metal Nanostructures: Synthesis, Assembly, and Their Applications in Electrochemistry. *Chem. Rev.*, **2015**, *115*, 8896–8943.
(42) X. Wang, J. Feng, Y. Bai, Q. Zhang and Y. Yin. Synthesis, Properties, and Applications of Hollow Micro-/Nanostructures. *Chem. Rev.*, **2016**, *116*, 10983−11060.
(43) X. W. Lou, L. A. Archer and Z. Yang. Hollow Micro-/Nanostructures: Synthesis and Applications. *Adv. Mater.*, **2008**, *20*, 3987–4019.
(44) G. Prieto, H. Tüysüz, N. Duyckaerts, J. Knossalla, G.-H. Wang and F. Schüth. Hollow Nano- and Microstructures as Catalysts. *Chem. Rev.*, **2016**, *116*, 14056−14119.
(45) P. Bhanja and A. Bhaumik. Porous nanomaterials as green catalyst for the conversion of biomass to bioenergy. *Fuel*, **2016**, *185*, 432–441.
(46) G. Tian, Y. Chen, W. Zhou, K. Pan, C. Tian, X.-R. Huang and H. Fu. 3D hierarchical flower-like TiO_2 nanostructure: morphology control and its photocatalytic property. *CrystEngComm*, **2011**, *13*, 2994–3000.
(47) D. J. Wales, J. Grand, V. P. Ting, R. D. Burke, K. J. Edler, C. R. Bowen, S. Mintova and A. D. Burrows. Gas sensing using porous materials for automotive applications. *Chem. Soc. Rev.*, **2015**, *44*, 4290–4321.
(48) X. Wang, W. Liu, J. Liu, F. Wang, J. Kong, S. Qiu, C. He and L. Luan. Synthesis of Nestlike ZnO Hierarchically Porous Structures and Analysis of Their Gas Sensing Properties. *ACS Appl. Mater. Interfaces*, **2012**, *4*, 817−825.
(49) F. Fan, Y. Feng, P. Tang, A. Chen, R. Luo and D. Li. Synthesis and Gas Sensing Performance of Dandelion-Like ZnO with Hierarchical Porous Structure. *Ind. Eng. Chem. Res.*, **2014**, *53*, 12737−12743.
(50) Q. Fu, M. Ai, Y. Duan, L. Lu, X. Tian, D. Sun, Y. Xu and Y. Sun. Synthesis of uniform porous NiO nanotetrahedra and their excellent gas-sensing performance toward formaldehyde. *RSC Adv.*, **2017**, *7*, 52312–52320.
(51) K. An and T. Hyeon. Synthesis and biomedical applications of hollow nanostructures. *Nano Today*, **2009**, *4*, 359–373.
(52) K. Cheng and S. Sun. Recent advances in syntheses and therapeutic applications of multifunctional porous hollow nanoparticles. *Nano Today*, **2010**, *5*, 183−196.
(53) L.-S. Lin, J. Song, H.-H. Yang and X. Chen. Yolk–Shell Nanostructures: Design, Synthesis, and Biomedical Applications. *Adv. Mater.*, **2018**, *30*, 1704639.
(54) A. Datt, N. Ndiege and S. C. Larsen. Development of Porous Nanomaterials for Applications in Drug Delivery and Imaging. In *Nanomaterials for Biomedicine*. R. Nagarajan, Ed. ACS Symposium Series; American Chemical Society: Washington, DC, 2012, pp. 239–258.
(55) J. Liu, D. Xue. Hollow Nanostructured Anode Materials for Li-Ion Batteries. *Nanoscale Res. Lett.*, **2010**, *5*, 1525–1534.
(56) Y. Zhao, M. Chen and L. Wu. Recent progress in hollow sphere-based electrodes for high-performance supercapacitors. *Nanotechnology*, **2016**, *27*, 342001.
(57) M.-H. Park, Y. Cho, K. Kim, J. Kim, M. Liu and J. Cho. Germanium Nanotubes Prepared by Using the Kirkendall Effect as Anodes for High-Rate Lithium Batteries. *Angew. Chem. Int. Ed.*, **2011**, *50*, 9647–9650.
(58) Q. Yun, Q. Lu, X. Zhang, C. Tan and H. Zhang. Three-Dimensional Architectures Constructed from Transition-Metal Dichalcogenide Nanomaterials for Electrochemical Energy Storage and Conversion. *Angew. Chem. Int. Ed.*, **2018**, *57*, 626–646.

(59) V. Sharma, I. Singh and A. Chandra. Hollow nanostructures of metal oxides as next generation electrode materials for supercapacitors. *Sci. Rep.*, **2018**, *8*, 1307.
(60) A. D. Smigelskas and E. O. Kirkendall. Zinc Diffusion in Alpha Brass. *Trans. AIME*, **1947**, *171*, 130–142.
(61) Y. Yin, R. Rioux, C. K. Erdonmez, S. Hughes, G. A. Somorjai and A. P. Alivisatos. Formation of Hollow Nanocrystals through the Nanoscale Kirkendall Effect. *Science*, **2004**, *304*, 711–714.
(62) W. Wang, M. Dahl and Y. Yin. Hollow Nanocrystals through the Nanoscale Kirkendall Effect. *Chem. Mater.*, **2013**, *25*, 1179–1189.
(63) H. J. Fan, U. Gçsele and M. Zacharias. Formation of Nanotubes and Hollow Nanoparticles Based on Kirkendall and Diffusion Processes: A Review. *Small*, **2007**, *3*, 1660–1671.
(64) C. Dong, D. Yao, J. Feng, T. Huang, X. Hu, Z. Wu, Y. Liu, B. Yang and H. Zhang. Facile Synthesis of Cu_2GeS_3 and Cu_2MGeS_4 (M = Zn, Mn, Fe, Co, and Ni) Hollow Nanoparticles, Based on the Nanoscale Kirkendall Effect. *Chem. Mater.*, **2016**, *28*, 9139–9149.
(65) C. Dong, R. Ge, D. Yao, Z. Wu, Z. Wang, Y. Liu, B. Yang and H. Zhang. Seed-mediated phase-selective growth of Cu_2GeS_3 hollow nanoparticles with huge cavities. *CrystEngComm*, **2017**, *19*, 6736–6743.
(66) L. Mu, F. Wang, B. Sadtler, R. A. Loomis and W. E. Buhro. Influence of the Nanoscale Kirkendall Effect on the Morphology of Copper Indium Disulfide Nanoplatelets Synthesized by Ion Exchange. *ACS Nano*, **2015**, *9*, 7419–7428.
(67) T. D. Ewers, A. K. Sra, B. C. Norris, R. E. Cable, C.-H. Cheng, D. F. Shantz and R. E. Schaak. Spontaneous Hierarchical Assembly of Rhodium Nanoparticles into Spherical Aggregates and Superlattices. *Chem. Mater.*, **2005**, *17*, 514–520.
(68) X. Ni, Q. Zhao, D. Zhang, X. Zhang and H. Zheng. Novel Hierarchical Nanostructures of Nickel: Self-Assembly of Hexagonal Nanoplatelets. *J. Phys. Chem. C*, **2007**, *111*, 601–605.
(69) Z. Zhang, X. Shao, H. Yu, Y. Wang and M. Han. Morphosynthesis and Ornamentation of 3D Dendritic Nanoarchitectures. *Chem. Mater.*, **2005**, *17*, 332–336.
(70) H. Wen, M. Cao, G. Sun, W. Xu, D. Wang, X. Zhang and C. Hu. Hierarchical Three-Dimensional Cobalt Phosphate Microarchitectures: Large-Scale Solvothermal Synthesis, Characterization, and Magnetic and Microwave Absorption Properties. *J. Phys. Chem. C*, **2008**, *112*, 15948–15955.
(71) C. Cannas, A. Ardu, A. Musinu, L. Suber, G. Ciasca, H. Amenitsch and G. Campi. Hierarchical Formation Mechanism of $CoFe_2O_4$ Mesoporous Assemblies. *ACS Nano*, **2015**, *9*, 7277–7286.
(72) X. Liang, Q. Cai, W. Xiang, Z. Chen, J. Zhong, Y. Wang, M. Shao and Z. Li. Preparation and Characterization of Flower-like Cu_2SnS_3 Nanostructures by Solvothermal Route. *J. Mater. Sci. Technol.*, **2013**, *29*, 231–236.
(73) M. Liu, G. Li, and X. Chen. One-Pot Controlled Synthesis of Spongelike $CuInS_2$ Microspheres for Efficient Counter Electrode with Graphene Assistance in Dye-Sensitized Solar Cells. *ACS Appl. Mater. Interfaces*, **2014**, *6*, 2604–2610.
(74) Y. Xie, C. Zhang, G. Yang, J. Yang, X. Zhou and J. Ma. Highly crystalline stannite-phase Cu_2XSnS_4 (X = Mn, Fe, Co, Ni, Zn and Cd) nanoflower counter electrodes for ZnO-based dye-sensitised solar cells. *J. Alloys Compd.*, **2017**, *696*, 938–946.
(75) J. Zhong, Q. Wang and W. Cai. Rapid synthesis of flower-like Cu_2CoSnS_4 microspheres with nanoplates using a biomolecule-assisted method. *Mater. Lett.*, **2015**, *150*, 69–72.

(76) J. Zhong, Q. Wang, D. Chen, L. Chen, H. Yu, H. Lu and Z. Ji. Biomolecule-assisted solvothermal synthesis of 3D hierarchical Cu_2FeSnS_4 microspheres with enhanced photocatalytic activity. *Appl. Surf. Sci.*, **2015**, *343*, 28–32.

(77) S. Yuan, S. Wang, L. Li, Y.-H. Zhu, X.-B. Zhang and J.-M. Yan. Integrating 3D Flower-Like Hierarchical Cu_2NiSnS_4 with Reduced Graphene Oxide as Advanced Anode Materials for Na-Ion Batteries. *ACS Appl. Mater. Interfaces*, **2016**, *8*, 9178−9184.

(78) W.-H. Zhou, Y.-L. Zhou, J. Feng, J.-W. Zhang, S.-X. Wu, X.-C. Guo and X. Cao. Solvothermal synthesis of flower-like Cu_2ZnSnS_4 nanostructures and their application as anode materials for lithium-ion batteries. *Chem. Phys. Lett.*, **2012**, *546*, 115–119.

(79) J. Xu, X. Yang, Q.-D. Yang, T.-L. Wong and C.-S. Lee. Cu_2ZnSnS_4 Hierarchical Microspheres as an Effective Counter Electrode Material for Quantum Dot Sensitized Solar Cells. *J. Phys. Chem. C*, **2012**, *116*, 19718−19723.

(80) Y.-L. Zhou, W.-H. Zhou, M. Li, Y.-F. Du and S.-X. Wu. Hierarchical Cu_2ZnSnS_4 Particles for a Low-Cost Solar Cell: Morphology Control and Growth Mechanism. *J. Phys. Chem. C*, **2011**, *115*, 19632–19639.

(81) X. Zhang, Y. Du, Z. Zhou and L. Guo. A simplified method for synthesis of band-structure-controlled $(CuIn)_xZn_{2(1-x)}S_2$ solid solution photocatalysts with high activity of photocatalytic H2 evolution under visible-light irradiation. *Int. J. Hydrog. Energy*, **2010**, *35*, 3313–3321.

(82) Y. Lin, F. Zhang and D. Pan. A facile route to $(ZnS)_x(CuInS_2)_{1-x}$ hierarchical microspheres with excellent water-splitting ability. *J. Mater. Chem.*, **2012**, *22*, 22619–22623.

(83) Z. An, J. Zhang, S. Pan and F. Yu. Facile Template-Free Synthesis and Characterization of Elliptic α-Fe_2O_3 Superstructures. *J. Phys. Chem. C*, **2009**, *113*, 8092–8096.

(84) Z. Zhang, H. Sun, X. Shao, D. Li, H. Yu and M. Han. Three-Dimensionally Oriented Aggregation of a Few Hundred Nanoparticles into Monocrystalline Architectures. *Adv. Mater.*, **2005**, *17*, 42–47.

(85) B. Jia, M. Qin, Z. Zhang, Z. Cao, H. Wu, P. Chen, L. Zhang, X. Lu and X. Qu. The formation of CuO porous mesocrystal ellipsoids via tuning the oriented attachment mechanism. *CrystEngComm*, **2016**, *18*, 1376–1383.

(86) R. L. Penn and J. A. Soltis. Characterizing crystal growth by oriented aggregation. *CrystEngComm*, **2014**, *16*, 1409–1418.

(87) V. K. Ivanov, P. P. Fedorov, A. Ye Baranchikov and V. V. Osiko. Oriented attachment of particles: 100 years of investigations of non-classical crystal growth. Russ. Chem. Rev., 2014, 83, 1204–1222.

(88) X. Xue, R. L. Penn, E. R. Leite, F. Huang and Z. Lin. Crystal growth by oriented attachment: kinetic models and control factors. *CrystEngComm*, **2014**, *16*, 1419–1429.

(89) M. D. Regulacio, S. Y. Tee, S. H. Lim, C. P. Teng, L.-D. Koh, S. Liu and M.-Y. Han. Facile solvothermal approach to pristine tetrahedrite nanostructures with unique multiply-voided morphology. *Nanoscale*, **2017**, *9*, 17865–17876.

(90) N. D. Petkovich and A. Stein. Controlling macro- and mesostructures with hierarchical porosity through combined hard and soft templating. *Chem. Soc. Rev.*, **2013**, *42*, 3721–3739.

(91) J.-J. Miao, L.-P. Jiang, C. Liu, J.-M. Zhu and J.-J. Zhu. General Sacrificial Template Method for the Synthesis of Cadmium Chalcogenide Hollow Structures. *Inorg. Chem.*, **2007**, *46*, 5673–5677.

(92) H. Wang, S. Zhuo, Y. Liang, X. Han and B. Zhang. General Self-Template Synthesis of Transition-Metal Oxide and Chalcogenide Mesoporous Nanotubes with Enhanced Electrochemical Performances. *Angew. Chem. Int. Ed.*, **2016**, *55*, 9055–9059.
(93) Y. Xin, Y. Huang, K. Lin, Y. Yu and B. Zhang. Self-template synthesis of double-layered porous nanotubes with spatially separated photoredox surfaces for efficient photocatalytic hydrogen production. *Sci. Bull.*, **2018**, *63*, 601–608.
(94) Y. Yu, Y. Huang, Y. Yu, Y. Shi and B. Zhang. Design of continuous built-in band bending in self-supported CdS nanorodbased hierarchical architecture for efficient photoelectrochemical hydrogen production. *Nano Energy*, **2018**, *43*, 236–243.
(95) Z. Su, C. Yan, D. Tang, K. Sun, Z. Han, F. Liu, Y. Lai, J. Li and Y. Liu. Fabrication of Cu_2ZnSnS_4 nanowires and nanotubes based on AAO templates. *CrystEngComm*, **2012**, *14*, 782−785.
(96) L. Shi, C. Pei and Q. Li. Ordered arrays of shape tunable $CuInS_2$ nanostructures, from nanotubes to nano test tubes and nanowires. *Nanoscale*, **2010**, *2*, 2126–2130.
(97) J. Lin, J.-M. Lim, D. H. Youn, K. Kawashima, J.-H. Kim, Y. Liu, H. Guo, G. Henkelman, A. Heller and C. B. Mullins. Self-Assembled Cu−Sn−S Nanotubes with High (De)Lithiation Performance. *ACS Nano*, **2017**, *11*, 10347−10356.
(98) L. Ai and J. Jiang. Self-sacrificial templating synthesis of porous quaternary Cu–Fe–Sn–S semiconductor nanotubes via microwave irradiation. *Nanotechnology*, **2012**, *23*, 495601.
(99) D. Wu, J. Duan, C. Zhang, K. Guo, and H. Zhu. Sacrificial Template Synthesis and Photothermal Conversion Enhancements of Hierarchical and Hollow $CuInS_2$ Microspheres. *J. Phys. Chem. C*, **2013**, *117*, 9121–9128.
(100) J. Zai, H. Chen, C. Huang, J. Huang, F. Chen, M. Xu and X. Qian. The fabrication of hollow cubic-like $CuInS_2$ cages using Cu_2O crystals as sacrificing template. *Mater. Chem. Phys.*, **2013**, *143*, 15−18.
(101) A. Zhang, Q. Ma, M. Lu, G. Yu, Y. Zhou and Z. Qiu. Copper–Indium Sulfide Hollow Nanospheres Synthesized by a Facile Solution-Chemical Method. *Cryst. Growth Des.*, **2008**, *8*, 2402−2405.
(102) Z. Zhang, Y. Fu, C. Zhou, J. Li and Y. Lai. EDTA-Na_2-assisted hydrothermal synthesis of Cu_2SnS_3 hollow microspheres and their lithium ion storage performances. *Solid State Ion.*, **2015**, *269*, 62−66.
(103) B. Qu, M. Zhang, D. Lei, Y. Zeng, Y. Chen, L. Chen, Q. Li, Y. Wang and T Wang. Facile solvothermal synthesis of mesoporous Cu_2SnS_3 spheres and their application in lithium-ion batteries. *Nanoscale*, **2011**, *3*, 3646–3651.
(104) H. You, L. Zhang, Y. Jiang, T. Shao, M. Li and J. Gong. Bubble-supported engineering of hierarchical $CuCo_2S_4$ hollow spheres for enhanced electrochemical performance. *J. Mater. Chem. A*, **2018**, *6*, 5265−5270.
(105) P. Ramasamy and J. Kim. Wurtzite Cu_2GeS_3 Nanocrystals: Phase- and Shape-Controlled Colloidal Synthesis. *Chem. Asian J.*, **2015**, *10*, 1468−1473.
(106) J.-H. Cha and D.-Y. Jung. $CuGaS_2$ hollow spheres from Ga–CuS core–shell nanoparticles. *Ultrason. Sonochem.*, **2014**, *21*, 1194−1199.
(107) Z. Bao, X. Liu, Y. Liu, H. Liu and K. Zhao. Near-infrared light-responsive inorganic nanomaterials for photothermal therapy. *Asian J. Pharm. Sci.*, **2016**, *11*, 349−364.
(108) J. Wang and N. Li. Functional hollow nanostructures for imaging and phototherapy of tumors. *J. Mater. Chem. B*, **2017**, *5*, 8430−8445.

(109) J. Z. Zhang. Biomedical Applications of Shape-Controlled Plasmonic Nanostructures: A Case Study of Hollow Gold Nanospheres for Photothermal Ablation Therapy of Cancer. *J. Phys. Chem. Lett.*, **2010**, *1*, 686–695.
(110) M. Song, N. Liu, L. He, G. Liu, D. Ling, X. Su and X. Sun. Porous hollow palladium nanoplatform for imaging-guided trimodal chemo-, photothermal-, and radiotherapy. *Nano Research*, **2018**, *11*, 2796–2808.
(111) L. Guo, D. D. Yan, D. Yang, Y. Li, X. Wang, O. Zalewski, B. Yan and W. Lu. Combinatorial Photothermal and Immuno Cancer Therapy Using Chitosan-Coated Hollow Copper Sulfide Nanoparticles. *ACS Nano*, **2014**, *8*, 5670–5681.
(112) S. Ramadan, L. Guo, Y. Li, B. Yan and W. Lu. Hollow Copper Sulfide Nanoparticle-Mediated Transdermal Drug Delivery. *Small*, **2012**, *8*, 3143–3150.
(113) G. Song, Q. Wang, Y. Wang, G. Lv, C. Li, R. Zou, Z. Chen, Z. Qin, K. Huo, R. Hu and J. Hu. A Low-Toxic Multifunctional Nanoplatform Based on Cu_9S_5@$mSiO_2$ Core-Shell Nanocomposites: Combining Photothermal- and Chemotherapies with Infrared Thermal Imaging for Cancer Treatment. *Adv. Funct. Mater.*, **2013**, *23*, 4281–4292.
(114) C. Yan, Q. Tian and S. Yang. Recent advances in the rational design of copper chalcogenide to enhance the photothermal conversion efficiency for the photothermal ablation of cancer cells. *RSC Adv.*, **2017**, 7, 37887–37897.
(115) S.-M. Zhou, D.-K. Ma, S.-H. Zhang, W. Wang, W. Chen, S.-M. Huang and K. Yu. PEGylated Cu_3BiS_3 hollow nanospheres as a new photothermal agent for 980 nm-laser-driven photothermochemotherapy and a contrast agent for X-ray computed tomography imaging. *Nanoscale*, **2016**, *8*, 1374–1382.
(116) G. Yu, A. Liu, H. Jin, Y. Chen, D. Yin, R. Huo, S. Wang and J. Wang. Urchin-Shaped Bi_2S_3/Cu_2S/Cu_3BiS_3 Composites with Enhanced Photothermal and CT Imaging Performance. *J. Phys. Chem. C*, **2018**, *122*, 3794−3800.
(117) Z. W. Seh, Y. Sun, Q. Zhang, Y. Cui. Designing High-Energy Lithium–Sulfur Batteries. *Chem. Soc. Rev.* **2016**, *45*, 5605–5634.
(118) M. Ge, X. Fang, J. Rong and C Zhou. Review of porous silicon preparation and its application for lithium-ion battery anodes. *Nanotechnology*, **2013**, *24*, 422001.
(119) S. L. Candelaria, Y. Shao, W. Zhou, X. Li, J. Xiao, J.-G. Zhang, Y. Wang, J. Liu, J. Li and G. Cao. Nanostructured carbon for energy storage and conversion. *Nano Energy*, **2012**, *1*, 195–220.
(120) W. Weng, J. Lin, Y. Du, X. Ge, X. Zhou and J. Bao. Template-free synthesis of metal oxide hollow micro-/nanospheres via Ostwald ripening for lithium-ion batteries. *J. Mater. Chem. A*, **2018**, DOI: 10.1039/c8ta03161d.
(121) C. Wang, E. Zhou, W. He, X. Deng, J. Huang, M. Ding, X. Wei, X. Liu and X. Xu. $NiCo_2O_4$-Based Supercapacitor Nanomaterials. *Nanomaterials*, **2017**, *7*, 41.
(122) C. Ding, Y. Zeng, L. Cao, L. Zhao and Q. Meng. Porous Fe_3O_4−NCs-in-Carbon Nanofoils as High-Rate and High-Capacity Anode Materials for Lithium-Ion Batteries from Na−Citrate-Mediated Growth of Super-Thin Fe−Ethylene Glycolate Nanosheets. *ACS Appl. Mater. Interfaces*, **2016**, *8*, 7977−7990.
(123) T. Liu, C. Jiang, W. You and J. Yu. Hierarchical porous C/MnO_2 composite hollow microspheres with enhanced supercapacitor performance. *J. Mater. Chem. A*, **2017**, *5*, 8635–8643.

(124) Z. Lu, N. Liu, H.-W. Lee, J. Zhao, W. Li, Y. Li and Y. Cui. Nonfilling Carbon Coating of Porous Silicon Micrometer-Sized Particles for High-Performance Lithium Battery Anodes. *ACS Nano*, **2015**, *9*, 2540–2547.
(125) Y. Zhao, X. Liu, H. Li, T. Zhai and H. Zhou. Hierarchical micro/nano porous silicon Li-ion battery anodes. *Chem. Commun.*, **2012**, *48*, 5079–5081.
(126) V. Etacheri, C. Wang, M. J. O'Connell, C. K. Chan and V. G. Pol. Porous carbon sphere anodes for enhanced lithium-ion storage. *J. Mater. Chem. A*, **2015**, *3*, 9861–9868.
(127) P. Kulkarni, S. K. Nataraj, R. Geetha Balakrishna, D. H. Nagaraju and M. V. Reddy. Nanostructured binary and ternary metal sulfides: synthesis methods and their application in energy conversion and storage devices. *J. Mater. Chem. A*, **2017**, *5*, 22040–22094.
(128) X. Y. Yu and X. W. Lou. Mixed Metal Sulfides for Electrochemical Energy Storage and Conversion. *Adv. Energy Mater.*, **2018**, *8*, 1701592.
(129) X. Rui, H. Tan and Q. Yan. Nanostructured metal sulfides for energy storage. *Nanoscale*, **2014**, *6*, 9889–9924.
(130) B. Qu, H. Li, M. Zhang, L. Mei, L. Chen, Y. Wang, Q. Li and T Wang. Ternary Cu_2SnS_3 cabbage-like nanostructures: large-scale synthesis and their application in Li-ion batteries with superior reversible capacity. *Nanoscale*, **2011**, *3*, 4389–4393.
(131) W. Zhang, H. Zeng, Z. Yang and Q. Wang. New strategy to the controllable synthesis of $CuInS_2$ hollow nanospheres and their applications in lithium ion batteries. *J. Solid State Chem.*, **2012**, *186*, 58–63.
(132) X. Yin, C. Tang, M. Chen, S. Adams, H. Wang and H. Gong. Hierarchical porous Cu_2ZnSnS_4 films for high-capacity reversible lithium storage applications. *J. Mater. Chem. A*, **2013**, *1*, 7927–7932.
(133) Y. Zeng, H. Li, B. Qu, B. Xiang, L. Wang, Q. Zhang, Q. Li, T. Wang and Y. Wang. Facile synthesis of flower-like Cu_3BiS_3 hierarchical nanostructures and their electrochemical properties for lithium-ion batteries. *CrystEngComm*, **2012**, *14*, 550–554.
(134) X. Gao, Y. Wang, Z. Ma, W. Jiang, Y. Zou and C. Lu. A ternary sulphonium composite Cu_3BiS_3/S as cathode materials for lithium–sulfur batteries. *J. Mater. Sci.*, **2016**, *51*, 5139–5145.
(135) Z. Sun, J. Zhang, L. Yin, G. Hu, R. Fang, H.-M. Cheng and F. Li. Conductive porous vanadium nitride/grapheme composite as chemical anchor of polysulfides for lithium-sulfur batteries. *Nat. Commun.*, **2017**, *8*, 14627.
(136) G. Li, J. Sun, W. Hou, S. Jiang, Y. Huang and J. Geng. Three-dimensional porous carbon composites containing high sulfur nanoparticle content for high-performance lithium–sulfur batteries. *Nat. Commun.*, **2016**, *7*, 10601.
(137) S. Cheng, T. Shi, C. Chen, Y. Zhong, Y. Huang, X. Tao, J. Li, G. Liao and Z. Tang. Construction of porous $CuCo_2S_4$ nanorod arrays via anion exchange for high-performance asymmetric supercapacitor. *Sci. Rep.*, **2017**, *7*, 6681.
(138) S. E. Moosavifard, S. Fani and M. Rahmanian. Hierarchical $CuCo_2S_4$ hollow nanoneedle arrays as novel binder-free electrodes for high-performance asymmetric supercapacitors. *Chem. Commun.*, **2016**, *52*, 4517–4520.
(139) Y. Zhu, X. Ji, H. Chen, L. Xi, W. Gong and Y. Liu. The investigation of the electrochemically supercapacitive performances of mesoporous $CuCo_2S_4$. *RSC Adv.*, **2016**, *6*, 84236–84241.

(140) Y. Tan, Z. Lin, W. Ren, W. Long, Y. Wang and X. Ouyang. Facile solvothermal synthesis of Cu_2SnS_3 architectures and their visible-light-driven photocatalytic properties. *Mater. Lett.*, **2012**, *89*, 240–242.
(141) C. Yu, L. Zhang, L. Tian, D. Liu, F. Chen and C. Wang. Synthesis and Formation Mechanism of $CuInS_2$ Nanocrystals with a Tunable Phase. *CrystEngComm*, **2014**, *16*, 9596–9602.
(142) K. Zhang, Y. Lin, C. Wang, B. Yang, S. Chen, S. Yang, W. Xu, H. Chen, W. Gan, Q. Fang, G. Zhang, G. Li and L. Song. Facile Synthesis of Hierarchical Cu_2MoS_4 Hollow Sphere/Reduced Graphene Oxide Composites with Enhanced Photocatalytic Performance. *J. Phys. Chem. C*, **2016**, *120*, 13120–13125.
(143) R. Rameshbabu, R. Vinoth, M. Navaneethan, Y. Hayakawa and B. Neppolian. Fabrication of Cu_2MoS_4 hollow nanotubes with rGO sheets for enhanced visible light photocatalytic performance. *CrystEngComm*, **2017**, *19*, 2475–2486.
(144) P. D. Tran, M. Nguyen, S. S. Pramana, A. Bhattacharjee, S. Y. Chiam, J. Fize, M. J. Field, V. Artero, L. H. Wong, J. Loo and J. Barber. Copper molybdenum sulfide: a new efficient electrocatalyst for hydrogen production from water. *Energy Environ. Sci.*, **2012**, *5*, 8912–8916.
(145) K. Zhang, Y. Zheng, Y. Lin, C. Wang, H. Liu, D. Liu, C. Wu, S. Chen, Y. Chen and L. Song. Designing hierarchical hollow nanostructures of Cu_2MoS_4 for improved hydrogen evolution reaction. *Phys. Chem. Chem. Phys.*, **2017**, *19*, 557–561.
(146) X. Lu, Y. Lin, H. Dong, W. Dai, X. Chen, X. Qu and X. Zhang. One-Step Hydrothermal Fabrication of Three-dimensional MoS_2 Nanoflower using Polypyrrole as Template for Efficient Hydrogen Evolution Reaction. *Sci. Rep.*, **2017**, *7*, 42309.
(147) Z. W. Seh, J. Kibsgaard, C. F. Dickens, I. Chorkendorff, J. K. Norskov, T. F. Jaramillo. Combining Theory and Experiment in Electrocatalysis: Insights into Materials Design. *Science* **2017**, *355*, eaad4998.
(148) J. Di, C. Yan, A. D. Handoko, Z. W. Seh, H. Li, Z. Liu. Ultrathin Two-Dimensional Materials for Photo- and Electrocatalytic Hydrogen Evolution. *Mater. Today* **2018**, DOI: 10.1016/j.mattod.2018.01.034.
(149) Z. Yang, S. Zhang, Y. Fu, X. Zheng and J. Zheng. Shape-controlled synthesis of $CuCo_2S_4$ as highly-efficient electrocatalyst for nonenzymatic detection of H_2O_2. *Electrochim. Acta*, **2017**, *255*, 23–30.
(150) X. Huang, G. Deng, L. Liao, W. Zhang, G. Guan, F. Zhou, Z. Xiao, R. Zou, Q. Wang and J. Hu. $CuCo_2S_4$ nanocrystals: a new platform for multi-modal imaging guided photothermal therapy. *Nanoscale*, **2017**, *9*, 2626–2632.
(151) B. Li, F. Yuan, G. He, X. Han, X. Wang, J. Qin, Z. Xiao Guo, X. Lu, Q. Wang, I. P. Parkin and C. Wu. Ultrasmall $CuCo_2S_4$ Nanocrystals: All-in-One Theragnosis Nanoplatform with Magnetic Resonance/Near-Infrared Imaging for Efficiently Photothermal Therapy of Tumors. *Adv. Funct. Mater.*, **2017**, *27*, 1606218.
(152) S. Chen and L.-W. Wang. Thermodynamic Oxidation and Reduction Potentials of Photocatalytic Semiconductors in Aqueous Solution. *Chem. Mater.*, **2012**, *24*, 3659−3666.
(153) R. Chetty, A. Bali and R. C. Mallik. Tetrahedrites as thermoelectric materials: an overview. *J. Mater. Chem. C*, **2015**, *3*, 12364–12378.
(154) J. Heo, G. Laurita, S. Muir, M. A. Subramanian and D. A. Keszler. Enhanced Thermoelectric Performance of Synthetic Tetrahedrites. *Chem. Mater.*, **2014**, *26*, 2047−2051.

(155) S. O. J. Long, A. V. Powell, P. Vaqueiro and S. Hull. High Thermoelectric Performance of Bornite through Control of the Cu(II) Content and Vacancy Concentration. *Chem. Mater.*, **2018**, *30*, 456−464.

(156) H. Ju, M. Kim, D. Park and J. Kim. Strategy for Low Thermal Conductivity and Enhanced Thermoelectric Performance in SnSe: Porous $SnSe_{1-x}S_x$ Nanosheets. *Chem. Mater.*, **2017**, *29*, 3228−3236.

(157) B. Xu, T. Feng, M. T. Agne, L. Zhou, X. Ruan, G. J. Snyder and Y. Wu. Highly Porous Thermoelectric Nanocomposites with Low Thermal Conductivity and High Figure of Merit from Large-Scale Solution-Synthesized $Bi_2Te_{2.5}Se_{0.5}$ Hollow Nanostructures. *Angew. Chem. Int. Ed.*, **2017**, *56*, 3546 –3551.

(158) O. Stroyuk, A. Raevskaya and N. Gaponik. Solar light harvesting with multinary metal chalcogenide nanocrystals. *Chem. Soc. Rev.*, **2018**, DOI: 10.1039/c8cs00029h.

(159) P. Dai, G. Zhang, Y. Chen, H. Jiang, Z. Feng, Z. Lin and J. Zhan. Porous copper zinc tin sulfide thin film as photocathode for double junction photoelectrochemical solar cells. *Chem. Commun.*, **2012**, *48*, 3006–3008.

(160) X. Zhang, X. Wu, A. Centeno, M. P. Ryan, N. M. Alford, D. J. Riley and F. Xie. Significant Broadband Photocurrent Enhancement by Au-CZTS Core-Shell Nanostructured Photocathodes. *Sci. Rep.*, **2016**, *6*, 23364.

(161) L. Zhou, Z. Zhuang, H. Zhao, M. Lin, D. Zhao and L. Mai. Intricate Hollow Structures: Controlled Synthesis and Applications in Energy Storage and Conversion. *Adv. Mater.*, **2017**, *29*, 1602914.

(162) Y. Si, M. Chen and L. Wu. Syntheses and biomedical applications of hollow micro-/nano-spheres with large-through-holes. *Chem. Soc. Rev.*, **2016**, *45*, 690–714.

Table 1. Porous CMS nanostructures synthesized through the different pore formation strategies.

Pore-forming Mode	Synthetic Method	CMS	Morphology, Size (if indicated)	Ref.
Kirkendall effect	Heating up	Cu_2GeS_3	Hollow spherical nanocrystals, 16.7 nm, pore size: 6.9 nm	64
	Hot-injection	Cu_2GeS_3	(a) Hollow spherical nanocrystals, ~10 nm (b) Hollow irregular-shaped nanostructures, 60–200 nm, wall thickness: 6 nm	65
	Hot-injection	$CuInS_2$	Hollow nanoplates, width: 46 nm, plate thickness: 13 nm	66
Aggregation	Solvothermal	Cu_2SnS_3	3D flowers, 1–1.5 μm, nanoflake thickness: 10 nm, nanocrystal unit: 3–5 nm	72
	Solvothermal	$CuInS_2$	3D sponge-like spheres, 0.8–3.7 μm, nanocrystal unit: 7–8 nm	73
	Solvothermal	Cu_3BiS_3	3D flowers, 1.5–3 μm	134
	Hydrothermal	$CuCo_2S_4$	3D flowers, 3 μm	149
	Solvothermal	Cu_2MSnS_4	3D flowers, 400 nm Note: M = Mn, Fe, Co, Ni, Zn, Cd	74
	Solvothermal	Cu_2CoSnS_4	3D flowers, ~1.5 μm	75
	Solvothermal	Cu_2FeSnS_4	3D spheres, 5–6 μm, nanosheet thickness: 100 nm	76
	Solvothermal	Cu_2NiSnS_4	3D flowers, several hundred nm	77
	Solvothermal	Cu_2ZnSnS_4	3D flowers, 1–2 μm, nanosheet thickness: 25 nm	78
	Solvothermal	Cu_2ZnSnS_4	3D spheres, ~2 μm, nanoflake thickness: 20 nm, nanocrystal unit: 3–5 nm	79
	Solvothermal	Cu_2ZnSnS_4	3D flowers, 500 nm, nanosheet thickness: 25 nm	80
	Hydrothermal	$(CuInS_2)_{1-x}(ZnS)_x$	3D spheres, 0.5 to several microns, nanocrystal unit: 15.6–41.6 nm	81
	Solvothermal	$(CuInS_2)_{1-x}(ZnS)_x$	3D spheres, 760 nm, nanocrystal unit: 8 nm	82
	Solvothermal	$Cu_{12}Sb_4S_{13}$	Multiply-voided nanotetrahedrons, 37 nm, void size: 3–20 nm	89
Hard-templating *(AAO template)*	Sol-gel + Annealing	Cu_2ZnSnS_4	Nanotubes, diameter: 200 nm, length: 60 μm	95
	Wet chemical	$CuInS_2$	Nanotubes and nano test tubes, diameter: 200 nm, wall thickness: 20 nm	96
Hard-templating *(sacrificial: CuCl−thiourea complex)*	Gelation + Solvothermal	Cu–Sn–S	Nanotubes with porous walls Note: Cu–Sn–S is a composite of Cu_2SnS_3, Cu_3SnS_4 and Cu_4SnS_4	97
	Microwave	Cu_2FeSnS_4	Nanotubes with porous walls, diameter: 400–800 nm, wall thickness: 100–200 nm, length: several microns	98
Hard-templating *(sacrificial: CuS)*	Solvothermal	$CuInS_2$	(a) 3D hollow spheres with flaky surface, 1 μm, shell thickness: 250 nm (b) 3D spheres with flaky surface, 1–1.2 μm	99
Hard-templating *(sacrificial: Cu_2GeS_3)*	Hot-injection	Cu_2MGeS_4	Hollow spherical nanocrystals, 15.4–16.8 nm, pore size: 4.4–5.7 nm Note: M = Mn, Fe, Co, Ni, Zn	64
Hard-templating *(sacrificial: Cu_2O)* + Kirkendall effect	Hydrothermal	$CuInS_2$	Hollow cubes with porous walls, 0.6–1 μm, wall thickness: 150 nm, void size: 250–600 nm	100
	Hydrothermal	$CuInS_2$	Hollow spheres with porous walls, 250 nm	131
	Solvothermal	Cu_2MoS_4	Hollow spheres with flaky surface (overall:	145

			flower-like), 100–150 nm	
Soft-templating	Wet chemical	$CuInS_2$	Hollow spheres with porous walls, 80–100 nm, some are peanut-shaped	101
Soft-templating *(CTAB)*	Hydrothermal	Cu_2SnS_3	Hollow spheres with porous walls, 1–1.2 μm, wall thickness: 0.2 μm	102
Soft-templating *(EDTA)*	Solvothermal	Cu_2SnS_3	3D mesoporous spheres, 200 nm	103
Soft-templating *(NH_3 and H_2S gas)*	Solvothermal	$CuCo_2S_4$	Hollow spheres with porous walls, 1–1.5 μm, wall thickness: 60–150 nm	104
Soft-templating *(H_2S gas)*	Hot-injection	Cu_2GeS_3	Hollow nanorectangles, width: 38.5 nm, length: 50 nm	105
Soft-templating *(sacrificial – Ga)*	Sonochemical	$CuGaS_2$	Hollow spheres with porous walls, 430 nm, wall thickness: 120 nm	106

Figures

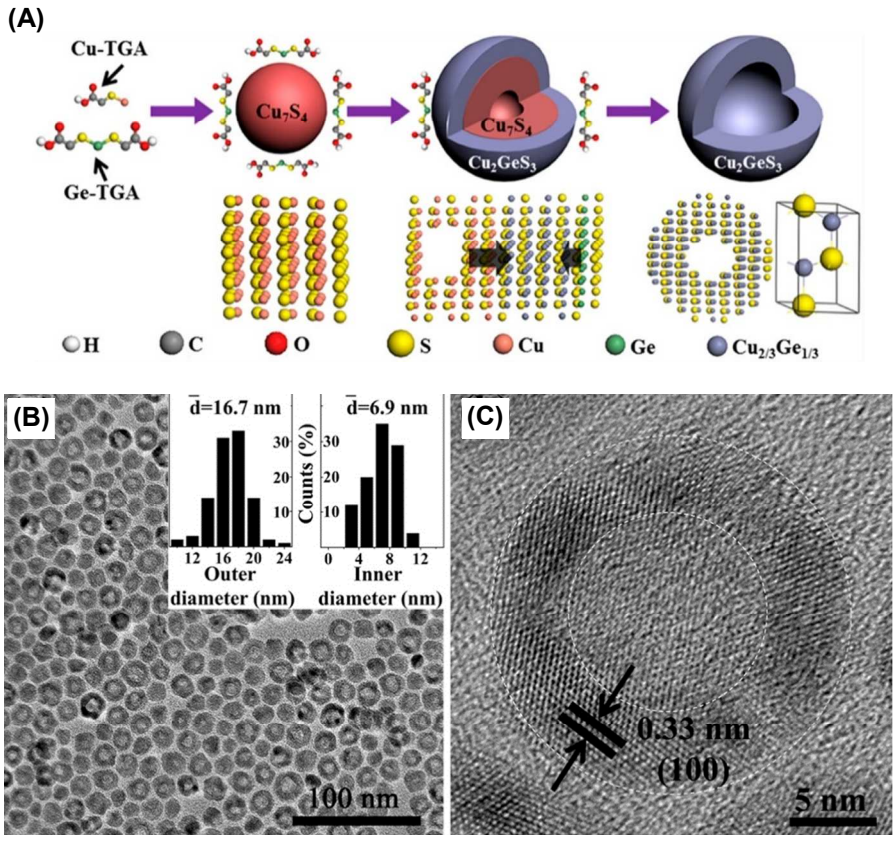

Figure 1. Kirkendall-effect-induced hollowing. (A) Schematic depiction of the mechanism of formation of hollow Cu_2GeS_3 nanostructures via the Kirkendall-type vacancy diffusion. (B) TEM and (C) HRTEM images of hollow Cu_2GeS_3 nanostructures. Reproduced with permission from ref. 64. Copyright 2016 American Chemical Society.

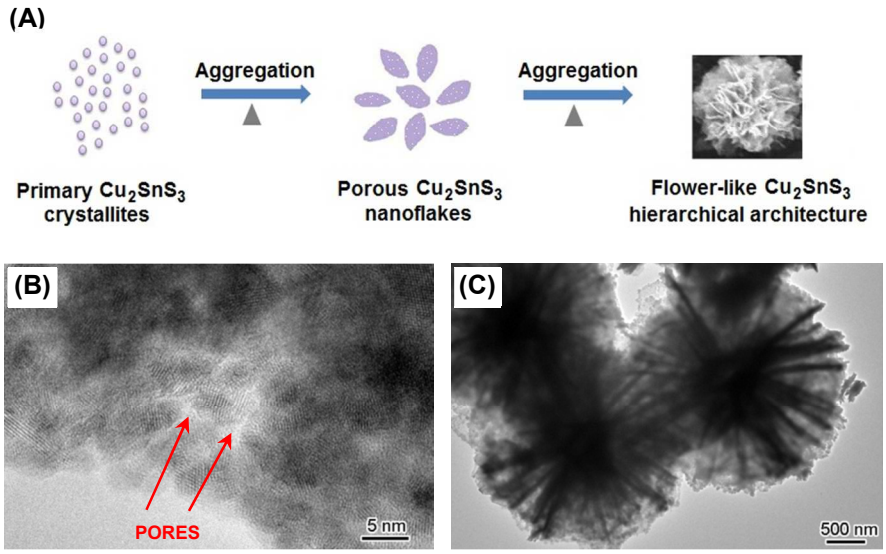

Figure 2. Aggregation-based pore formation leading to 3D hierarchical architectures. (A) Schematic illustration of the growth mechanism of mesoporous flower-like Cu_2SnS_3 architectures through a two-step aggregation process. (B) HRTEM image of a Cu_2SnS_3 nanoflake showing its polycrystalline nature and porous structure. (C) TEM image of Cu_2SnS_3 flower-like architectures. Adapted with permission from ref. 72. Copyright 2013 Elsevier.

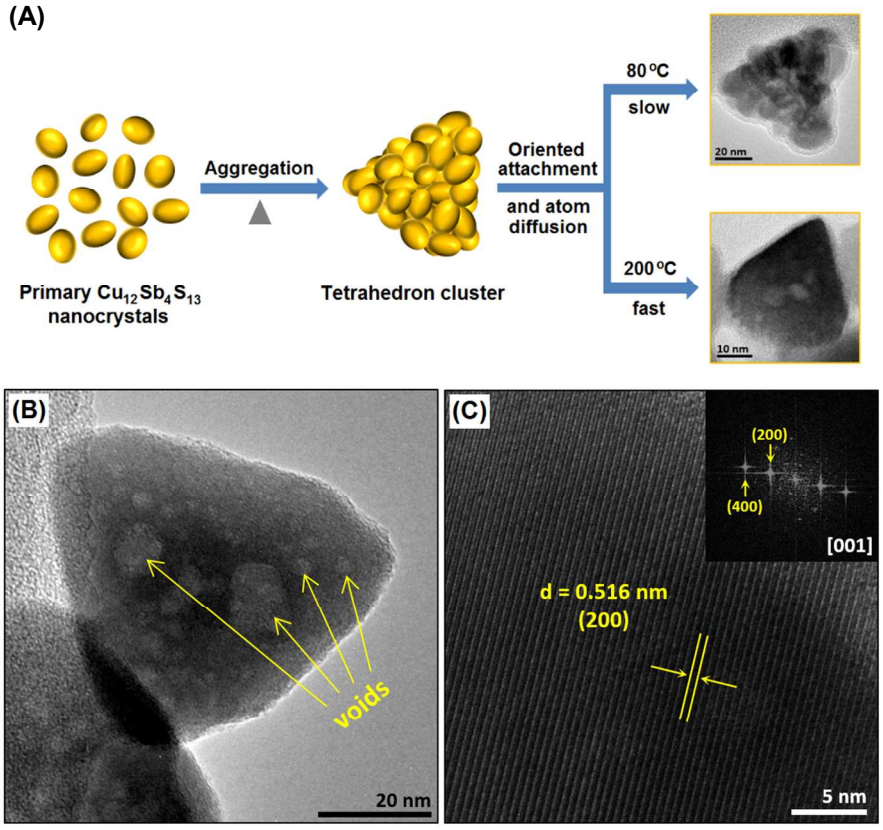

Figure 3. Aggregation-based pore formation leading to single-crystalline multiply-voided structures. (A) Pictorial representation of the growth mechanism of multiply-voided $Cu_{12}Sb_4S_{13}$ nanotetrahedrons through oriented attachment of smaller oval-shaped $Cu_{12}Sb_4S_{13}$ nanocrystals. (B) TEM and (C) HRTEM images of the $Cu_{12}Sb_4S_{13}$ nanotetrahedrons produced at 200 °C. The sphere-like voids are highlighted in (B) while the single-crystallinity is shown in (C). Reproduced with permission from ref. 89. Copyright 2017 The Royal Society of Chemistry.

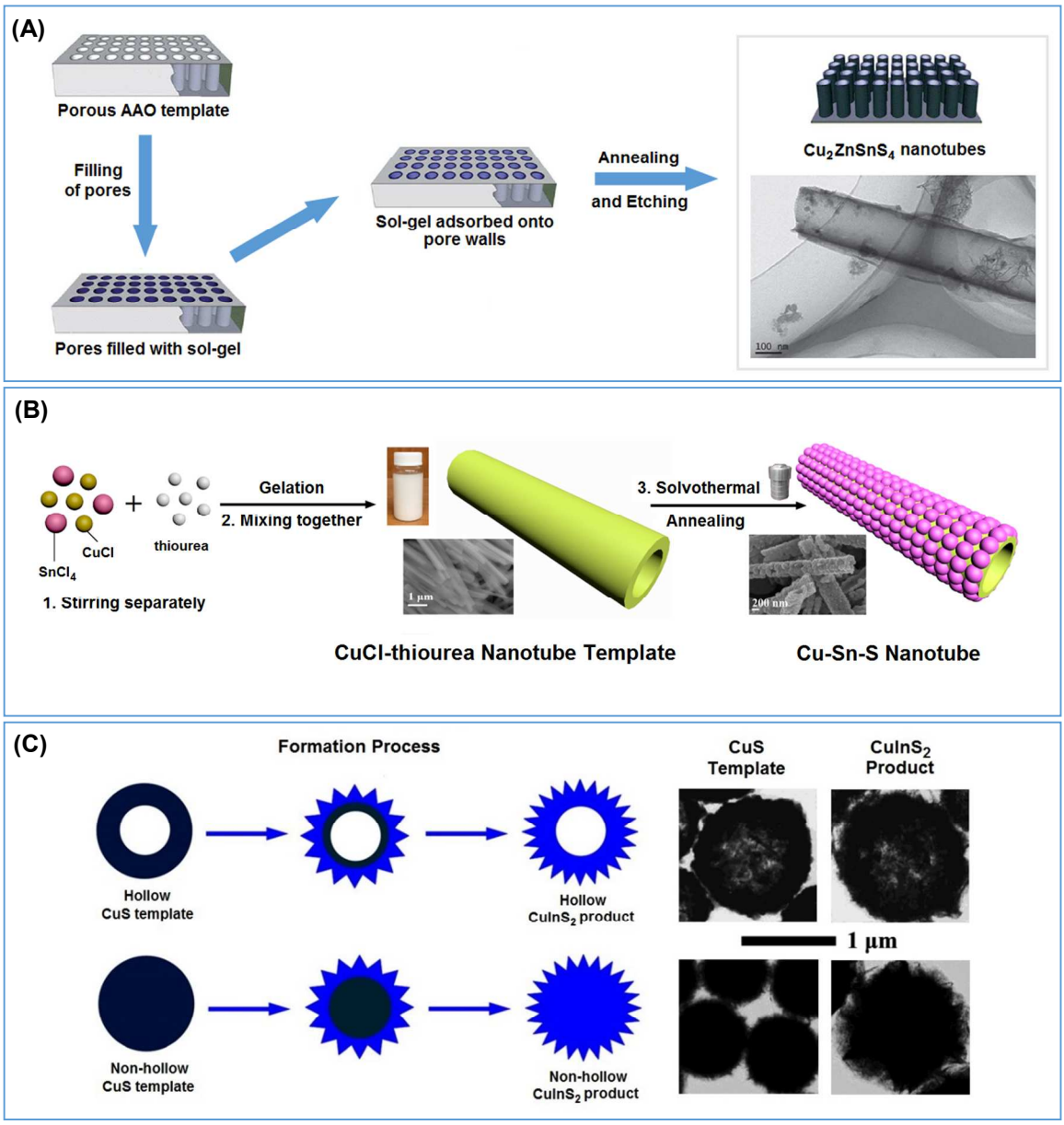

Figure 4. Pore engineering using hard templates. (A) Schematic diagram of the formation process of Cu_2ZnSnS_4 nanotubes using porous anodic aluminum oxide (AAO) template. Adapted with permission from ref. 95. Copyright 2011 The Royal Society of Chemistry. (B) Schematic diagram showing the formation of porous Cu–Sn–S nanotubes from *in situ* generated CuCl–thiourea nanotube template. Reproduced with permission from ref. 97. Copyright 2017 American Chemical Society. (C) Schematic illustration of the formation of porous architectures of $CuInS_2$ from CuS templates. TEM images of the templates and the products are also shown. Adapted with permission from ref. 99. Copyright 2013 American Chemical Society.

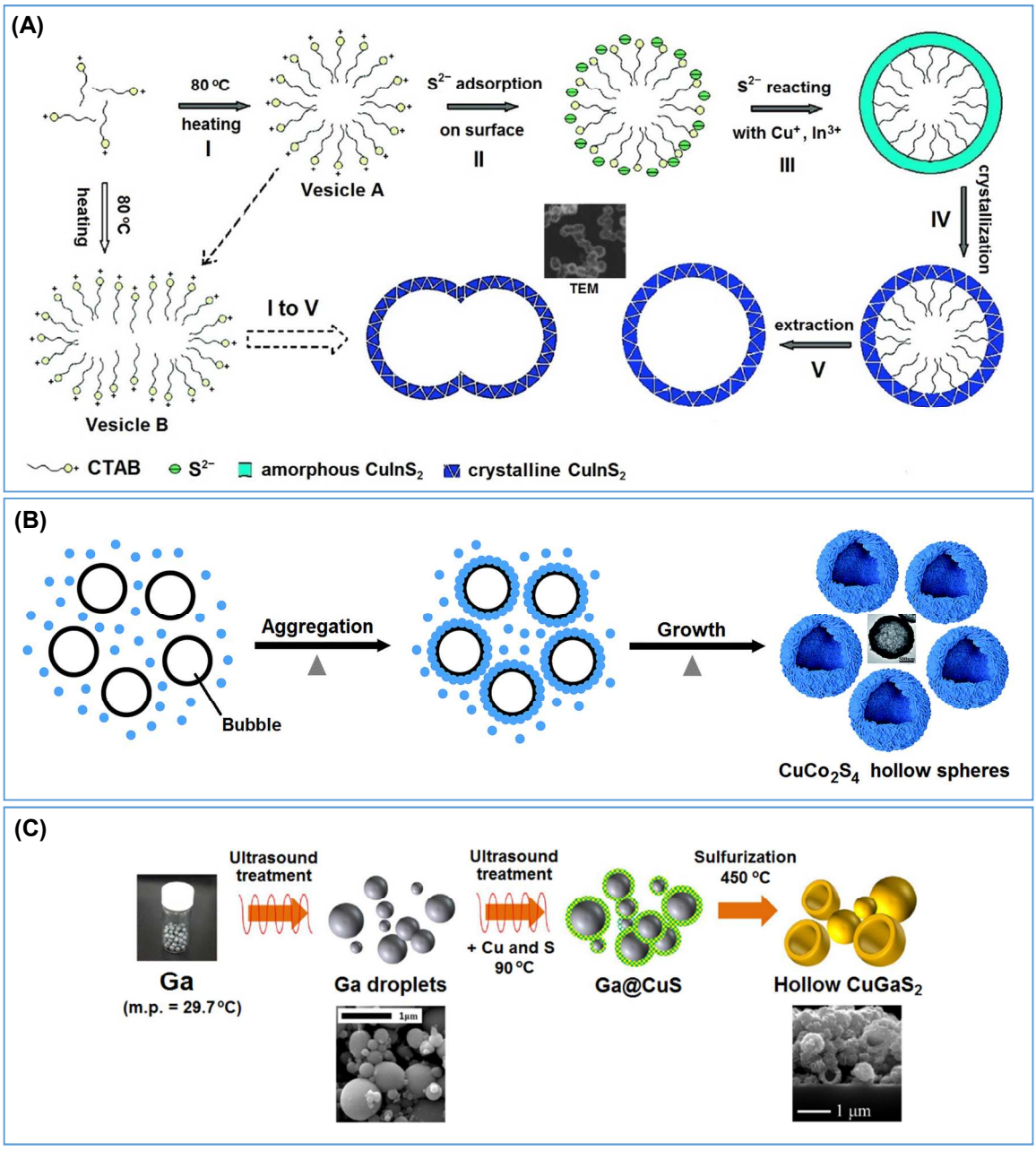

Figure 5. Pore engineering using soft templates. (A) Schematic depiction of the formation process of hollow $CuInS_2$ architectures using surfactant vesicles. Adapted with permission from ref. 101. Copyright 2008 American Chemical Society. (B) Schematic illustration of the growth of hollow $CuCo_2S_4$ spheres via a bubble template mechanism. Adapted with permission from ref. 104. Copyright 2017 The Royal Society of Chemistry. (C) Schematic diagram showing the formation of hollow $CuGaS_2$ spheres using Ga droplets as a reactive fluid template. Adapted with permission from ref. 106. Copyright 2014 Elsevier.

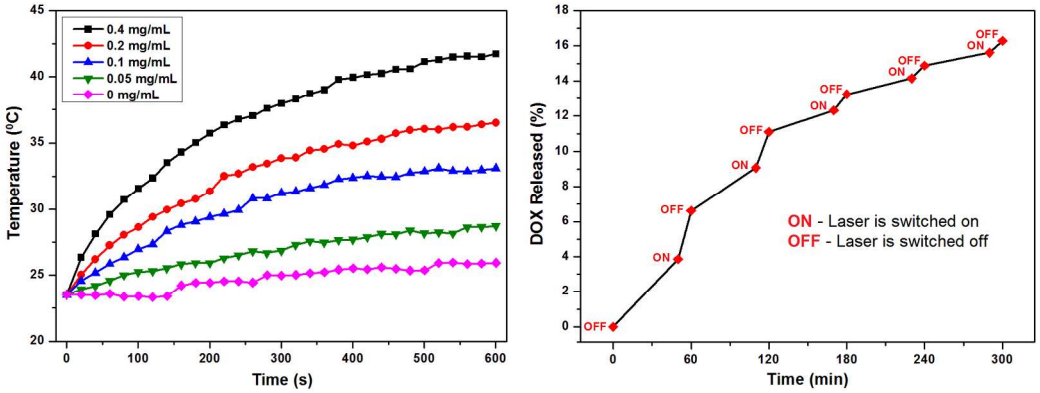

Figure 6. Left: Concentration-dependent photothermal heating of MPA-capped porous $Cu_{12}Sb_4S_{13}$ nanotetrahedrons in water under 808-nm laser irradiation. Right: Photothermal-mediated DOX release from porous $Cu_{12}Sb_4S_{13}$ nanotetrahedrons at pH 4.8. Reproduced with permission from ref. 89. Copyright 2017 The Royal Society of Chemistry.

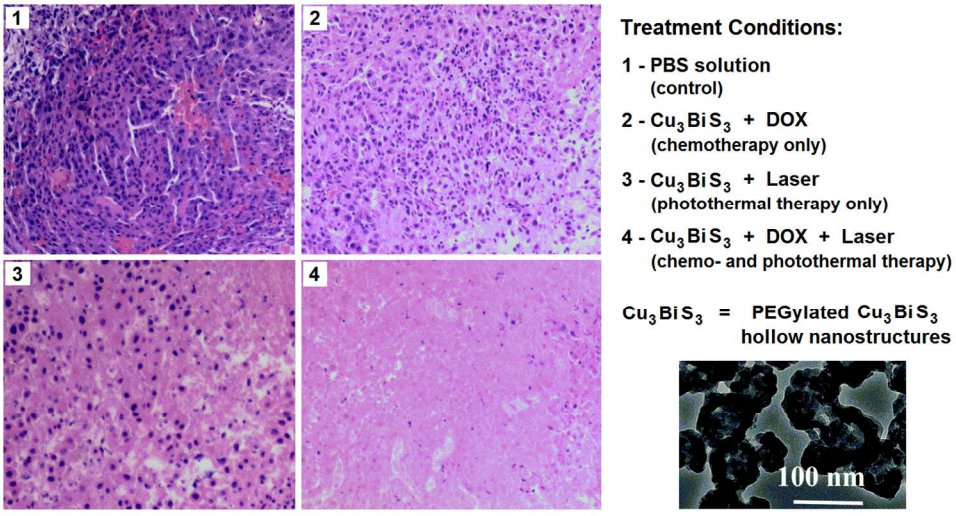

Figure 7. Hematoxylin–eosin stained histological images of tumor tissues from melanoma-bearing mice treated under different conditions. TEM image of the PEGylated Cu_3BiS_3 hollow nanostructures is also shown. Reproduced with permission from ref. 115. Copyright 2015 The Royal Society of Chemistry.

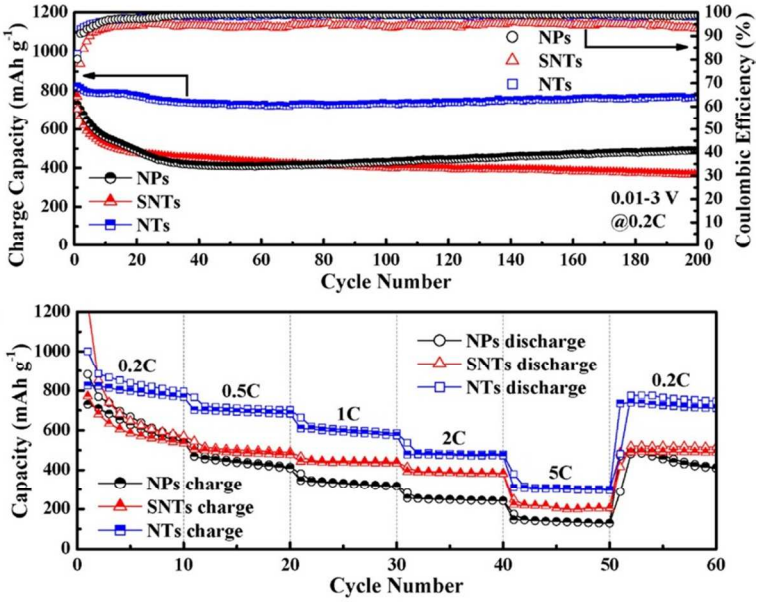

Figure 8. Comparison of cycling performance (top) and rate capability (bottom) of Cu–Sn–S nanotubes (NTs), sub-nanotubes (SNTs), and nanoparticles (NPs). Reproduced with permission from ref. 97. Copyright 2017 American Chemical Society.

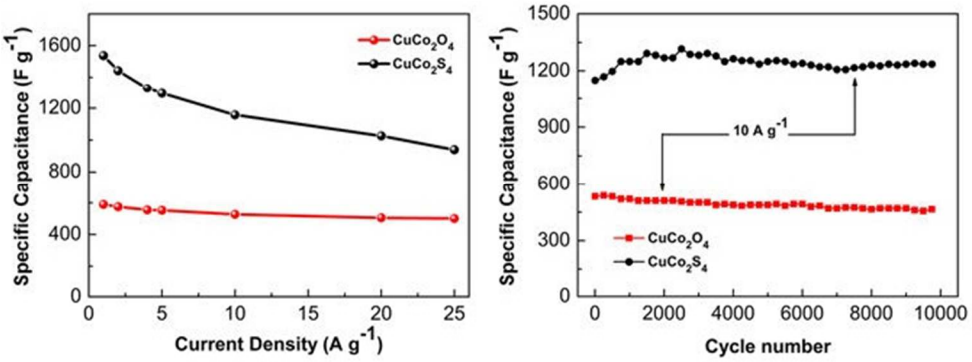

Figure 9. Comparison of specific capacitance as a function of current density (left) and cycling performance (right) of mesoporous $CuCo_2S_4$ and $CuCo_2O_4$ array electrodes. Reproduced with permission from ref. 137. Copyright 2017 Springer Nature.

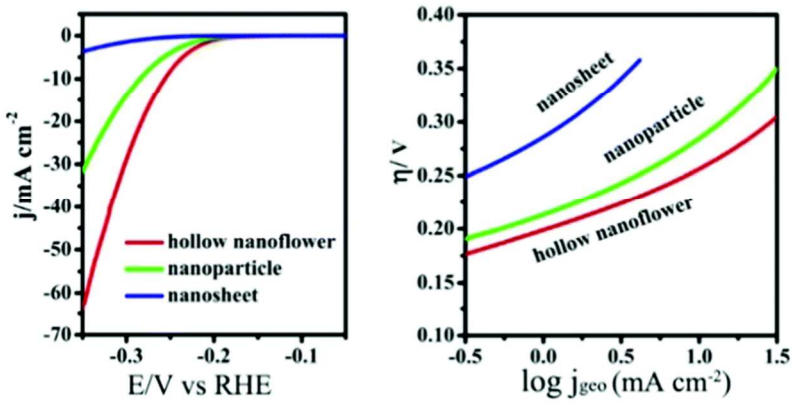

Figure 10. Comparison of the polarization (left) and Tafel (right) curves of hydrogen evolution reaction (HER) electrodes based on different Cu_2MoS_4 nanostructures: hollow nanoflowers, nanosheets and nanoparticles. Reproduced from ref. 145 with permission from the PCCP Owner Societies. Copyright 2016 The Royal Society of Chemistry.

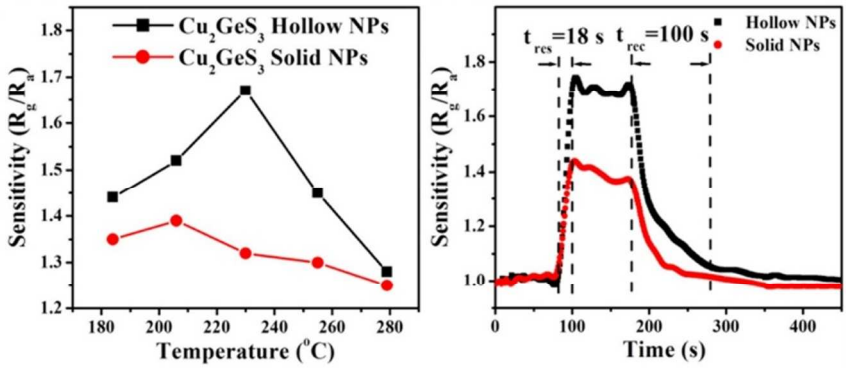

Figure 11. Comparison of the sensing response of hollow and solid (non-hollow) Cu_2GeS_3 nanoparticles (NPs) toward 5 ppm ethanol gas in air as a function of operating temperature (left), and their response transient curves at their optimum operating temperature (right). Reproduced with permission from ref. 64. Copyright 2016 American Chemical Society.

TOC Graphic

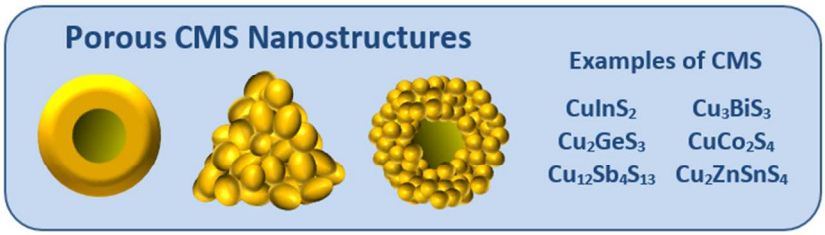
Porous CMS Nanostructures
Examples of CMS
$CuInS_2$
Cu_3BiS_3
Cu_2GeS_3
$CuCo_2S_4$
$Cu_{12}Sb_4S_{13}$
Cu_2ZnSnS_4